SETCOR
Conferences & Exhibitions

The Nanotech Middle East 2027 International Conference

Nanotech ME 2017

December 4 to 6, 2017, Dubai - UAE

Conference Proceedings

DOI: https://doi.org/10.26799/cp-nanotechme2017

Proceedings of the Nanotech Middle East 2017 International Conference
Dubai, UAE – December 4 – 6, 2017
DOI: https://doi.org/10.26799/cp-nanotechme2017

Microanalysis of Interfacial Transition Zone between Surface Modified Polymeric Fibres and Cement Matrix

Zdeněk Prošek[1], Jan Trejbal[2], Zuzana Rácová[3], Aleš Jíra[4]
[1]Czech Technical Unversity in Prague, Faculty of Civil Engineering, Department of Mechanics, Prague, Czech Republic, EU, zdenek.prosek@fsv.cvut.cz
[2]Czech Technical Unversity in Prague, Faculty of Civil Engineering, Department of Mechanics, Prague, Czech Republic, EU, jan.trejbal@fsv.cvut.cz
[3]Czech Technical Unversity in Prague, Faculty of Civil Engineering, Department of Mechanics, Prague, Czech Republic, EU, zuzana.racova@fsv.cvut.cz
[4]Czech Technical Unversity in Prague, Faculty of Civil Engineering, Department of Mechanics, Prague, Czech Republic, EU, ales.jira@fsv.cvut.cz

Abstract
In the field of composite materials, an interface interaction is a crucial parameter influencing of bulk properties of them. This phenomena is very important namely in the case of polymer fibre reinforced cement composites. Standardly used polymer fibres exhibit smooth and chemically inert surfaces. Consequently, a strong interaction between them and cement matrix is not ensured. We tried to modify two widespread polymer macro fibres having ca. 0.5 mm in a diameter in order to change their surfaces from hydrophobic to hydrophilic and from smooth to roughened. To attain a target goal, we exposed them to the low-pressure cold plasma treatment. Thus modified fibres we used as reinforcement of cement samples composed of CEM I 42.5R (w/c 0.4). Then, we prepared rigorously polished section from them at which we studied the ITZ zone. We focused namely on the chemical composition of the ITZ. Elements maps of the ITZ were composed by means of an energy-dispersive (EDS) and the wave-dispersive (WDS) spectroscopy analyser. Mechanical properties of the ITZ were examined using nanoindentation technique. ITZs around reference fibres were compared with those around treated fibres. We found out, that between them, there were a significant difference in an amount of elements like Ca, Si and C. An occurrence of mentioned elements was higher in cement paste samples containing treated fibres than in the case of reference samples. Certain changes were also observed in the mechanical properties of the ITZ. It was shown, that the reduced modulus of elasticity was significantly higher in the case of treated samples.

Keywords: polymeric fibre, surface properties, plasma, interfacial transition zone, cement matrix, microanalysis, nanoindentation

1. Introduction

The polymeric fibre reinforcement becomes popular in the field of composite materials due to its favourable properties as low cost, mechanical performance, chemical stability and the like [1-3]. Unfortunately, as it has been mentioned many times, a surface of the most of polymeric fibres (e.g. poly-ethylene terephthalate, polypropylene, poly-ethylene, etc.) can be described as smooth and rather hydrophobic. These facts may limit a potential of composite materials due to insufficient both the chemical and the physical interaction between them and continual phases. This phenomenon is perceptible in the field of civil engineering industry, where fibre composite materials based on cement matrixes are often used. An unsatisfactory chemical interaction between polymer fibres and cement matrix results on a poor bond and even on an estimation of porous areas in interfacial transition zones (ITZ), as illustrated on Fig. 1 [3-5]. In fibre reinforced concrete, the ITZ zone is one of four basic phases (other ones are aggregate, cement matrix, reinforcement). Its thickness is about 15-50 μm. Fibre-matrix bond properties play an important role in determining concrete properties. It is obvious that the ITZ having poor mechanical properties does not allow an effective stress transport from matrix to reinforcement. A principle of a synergic interaction between composite phases is thus no guaranteed [6-8].
To eliminate the mentioned phenomenon, the fibre surface treatment should be done. It is desirable to change fibre surfaces from hydrophobic to hydrophilic and from smooth to roughen [3, 4, 8]. Cement binders contain water (polar liquid); therefore it is desirable to activate the fibre surface and thus to guarantee the strong chemical bond between the two materials. However, in some cases, there is a mechanical interaction rather than the chemical required [5]. Therefore, the fibre surface should be roughened to increase an interface shear stress between the two materials.

DOI: https://doi.org/10.26799/cp-nanotechme2017

There are a few ways based on the chemical (surface activation and etching) and the physical (roughening) treatment [1, 9-11]. Besides, these ways can be combined, e.g. by a plasma treatment. The cold low pressure plasma treatment in an oxygen atmosphere seems to be an effective alternative to modify polymer fibre surfaces chemically as well as physically. The chemical modification rests in surface activation via an implementation of an active polar group, while the physical treatment is realised via ion bombardment. The bond between in this manner treated fibres and the cement matrix is stronger. Moreover, due to fibre surfaces roughening, the interfacial shear stress between them and the matrix is increased [5, 12].
Within this study, we modified polymer macro-fibres by means of the low-pressure oxygen cold plasma. Subsequently, we made cement samples reinforced with the treated fibres to examine properties of the ITZ. Mechanical parameters of the ITZ was investigated using the nanoindentation, while its chemical composition was studied by SEM phase analysis.

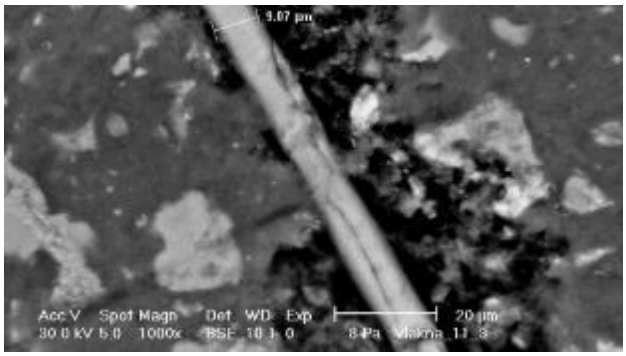

Fig. 1: SEM image of porous structure of ITZ between PET fibre and cement matrix.

2. Materials and Samples

2.1. Fibres

Two types of polymer macro fibres were used to improve their surfaces – coated and uncoated. A choice of these specific types were subjected to represent the most widespread fibres in the field of civil engineering. Coated fibres are composed from two components – load bearing core and protective shell, while the uncoated are mono-component. A manufacturer of coated fibres did not provide any detailed information about their chemical composition. Basic bulk fibre parameters are summarized in the Table 1.

Table 1: Basic parameters of tested fibres.

Fibre type	Material	Density [g/cm^3]	Diameter [mm]	Length [mm]	Tensile Strength [N/mm^2]	Young's Modulus of Elasticity [GPa]
Coated	Polyolefin	900	0.5	50	600	>10
Uncoated	PP+PE	910	0.48	55	610	5.17

2.2. Cement paste samples

As received and plasma treated fibres were mixed into a cement paste. The paste composed from Portland cement CEM I 42.5R, water to cement ratio was equal to 0.4. An amount of fibres was 2 % of the sample volume. Prismatic samples were made from the mixture using metal forms. Hereby prepared samples were cast out after 24 hours from forms and stored submerged into water for 27 days. After that, samples were cross-cut by means of a circular saw with a diamond disc in order to attain well-prepared seams. The perfect treated surface of the cross-section is crucial to attain accurate results; therefore, they were next polished using the Tegramin polishing machine (Struers) in a few steps, when the final step was executed via a polishing rotary screen with nano-diamond particles (size: 500-4000 grains./cm^2 of the functional area).

3. Materials and Samples

DOI: https://doi.org/10.26799/cp-nanotechme2017

3.1. Plasma Treatment

In order to modify fibre surfaces, the low-pressure cold inductively coupled plasma treatment in the oxygen atmosphere was done. Parameters of the process were as follows: machine Tesla VT 214, frequency and power was 13.56 MHz and 100 W, respectively, total gas pressure 60 Pa, oxygen flow 50 sccm, treatment time 480 seconds.

3.2. SEM Element Analysis

The element analysis of the ITZ was realised using the SEM microscope Merlin (Zeiss) equipped with an energy-dispersive (EDS) and a wave-dispersive (WDS) spectroscopy analyser. Settings of the whole process was following: EHT 10 kV, probe electricity 200 pA, work table distance 8.5 mm, frame count 30, time to frame 79 seconds, pixel dwell time 100 µs and resolution 1024 px.

3.3. Nanoindentation

To assess mechanical properties of the ITZ, the nanoindentation was done using the nanoindenter Ti 700 (Hysitron). Berkovich shape type of an indentation probe was used. Mechanical parameters were assessed from an unloading part during loading. Two matrixes about the total number of 56 indents (14×4) were performed; each matrix was placed close to the edge of the fibre, as imagined in the Fig. 2. A distance between indents was 15 µm. The indentation force was 15 mN.

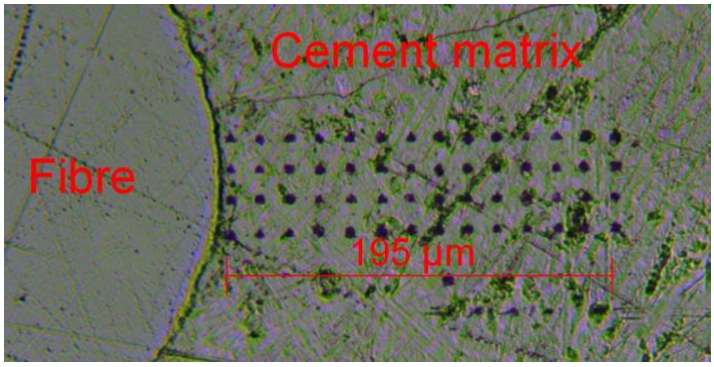

Fig. 2: Indentation matrix.

4. Results

4.1. SEM Element Analysis

To assess composition changes on the ITZ, the elements map of them was composed. In both, reference (the ITZ between as received fibres) and treated samples (containing 480 seconds plasma treated fibres), following elements were detected: Fe, Ca, Mg, Na, K, P, S, Al, Si, O, C. The most significant changes were found in the case of element Ca, Si and C. Fig. 3 shows an occurrence of the Ca. It could be said, that in surroundings of reference fibres, there is relatively low concertation of the Ca than in treated samples. Similarly, the amount of the Si is higher in the case of samples with treated fibres than those with reference ones, as captured in the Fig. 4. The same phenomena was analysed also for the concertation of the C, see Fig. 5. In all cases, the increased amount of each of the element was detected in the distance from 0 to 80 µm from the fibre edge.

DOI: https://doi.org/10.26799/cp-nanotechme2017

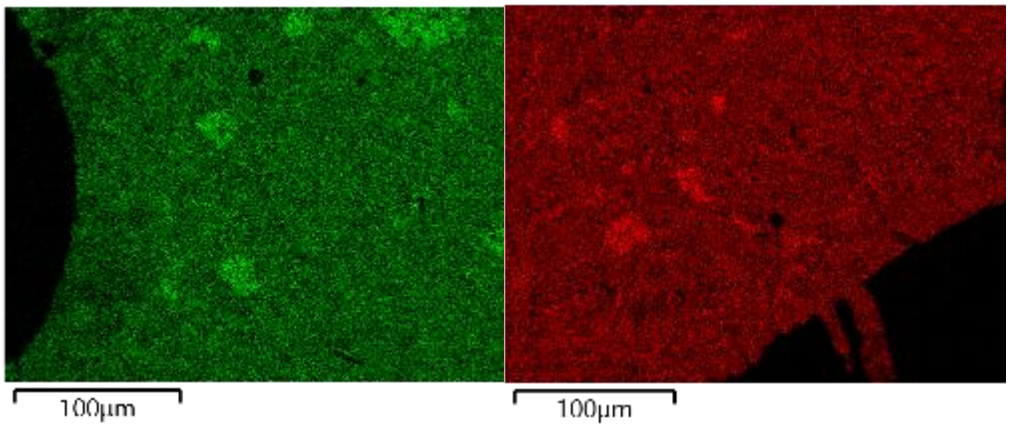

Fig. 3: Occurrence of the Ca through the ITZ around the reference (left) and treated fibre (right).

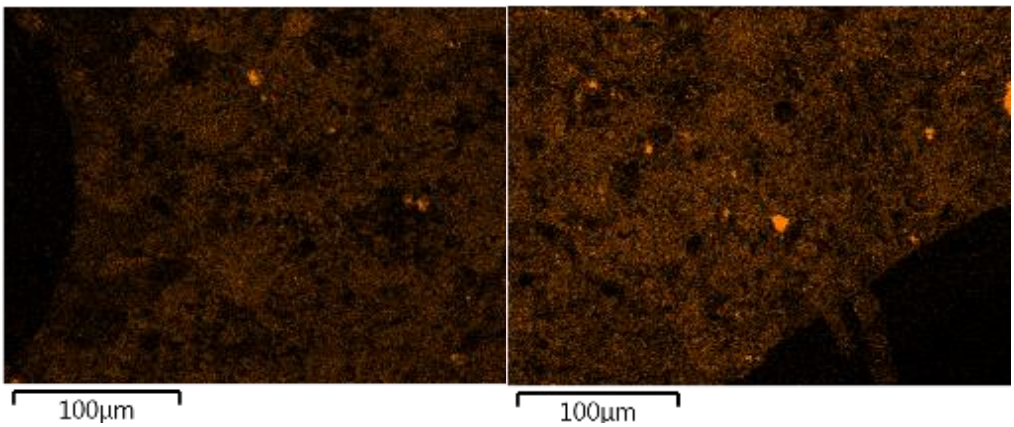

Fig. 4: Occurrence of the Si through the ITZ around the reference (left) and the treated fibre (right).

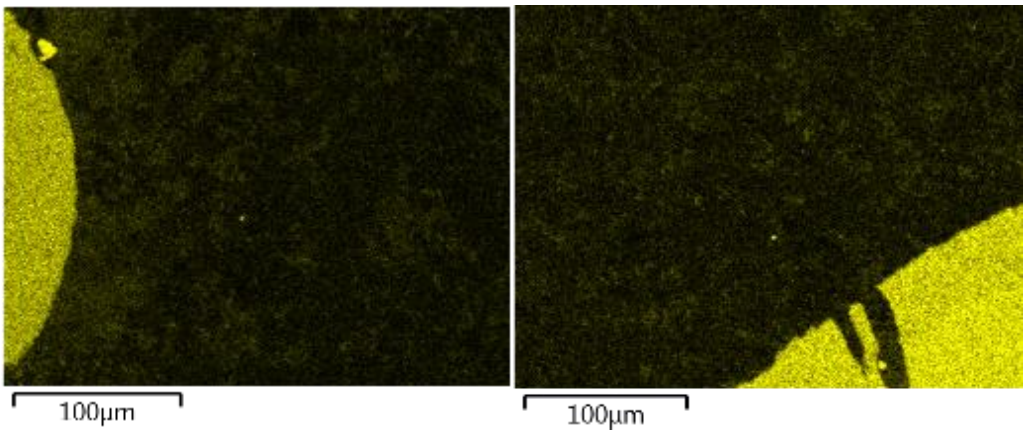

Fig. 5: Occurrence of the C through the ITZ around the reference (left) and the treated fibre (right).

4.2. Nanoindentation

It was expected, that the modulus of elasticity of the ITZ around treated fibres will be higher than those in the vicinity of reference fibres. This phenomena was indeed proven. The Fig. 6 clearly shows that the toughness of the ITZ of the treated sample is higher if compared to reference one. The increased toughness was detected over the entire length of the track. By focusing on the distance of 60-80 µm, it was found out, that the reduced modulus of elasticity oscillated between ca. 33-42 GPa and 22-28 GPa in the case of treated a reference fibres, respectively.

DOI: https://doi.org/10.26799/cp-nanotechme2017

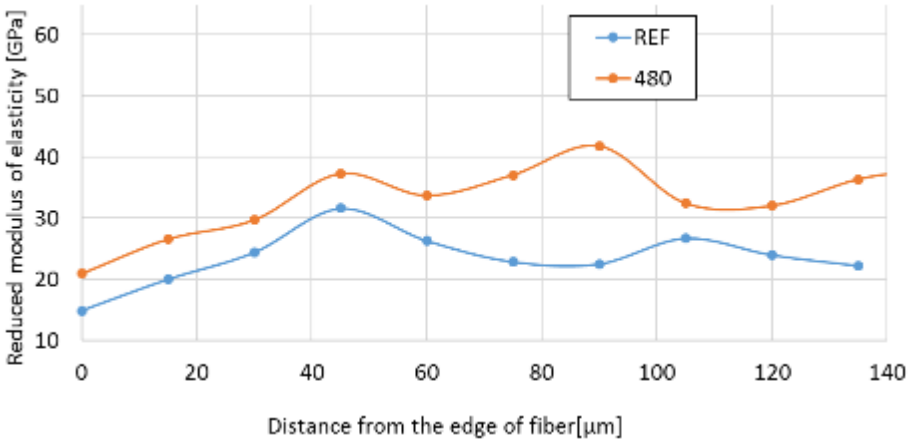

Fig. 6: Reduced modulus of elasticity as a function of distance from fibre edge in ITZ.

5. Conclusion

This work deals with the surface modification of polymer macro fibres in order to change their surface properties and thus to ensure a strong bond between them and the cement matrix. For purposes of the modification, we used two type of commonly used polymer macro fibres having ca. 0.5 mm in diameter. The first type was bi-component polyolefin fibres composes of load-bearing core and protecting shell, while the second type was monolayer composed from mixture of PP and PE. To change their surface from smooth to slightly roughened and from water hydrophobic to hydrophilic, we treated them via the cold low-pressure oxygen plasma. This modification should improve mechanical parameters of the ITZ between fibre surfaces and the cement matrix. We came from the assumption, that the higher bond strength between the two materials, the higher mechanical properties of composite materials.

To answer the question how the treatment influence the ITZ, we made cement paste samples composed from Portland cement CEM I 42.5R (w/c 0.4) containing reference and 480 seconds plasma treated fibres. We prepared polished seams from them, while we focused on the ITZ between the two materials. The element analysis of the ITZ was realised using the SEM microscope Merlin (Zeiss) equipped with an energy-dispersive (EDS) and a wave-dispersive (WDS) spectroscopy analyser. Moreover, mechanical parameters of the ITZ were researched by means of the nanoindentation technology.

It can be concluded, that the ITZs around treated fibres contain a higher amount of elements like Ca, Si and C, if compared to them around reference fibres. A significant change of ITZ mechanical properties was also detected. The reduced modulus of elasticity of reference samples obtained using the nanoindentation between distances of 0-100 µm by the fibre reached maximally 32 GPa, samples containing treated fibres exhibited up to 42 GPa.

It can be concluded, that the plasma treatment of polymeric fibres has a significant impact on the ITZ between them and the cement matrix. As it was shown within this study, that the plasma treatment may eliminate polymer fibre drawbacks such as the smooth and the chemically inert surface. The fibre reinforced concrete may, thanks to this, get better mechanical properties due to the improvement of the ITZ.

Acknowledgements

This work was financially supported by Czech Technical University in Prague – SGS projects SGS16/201/OHK1/3T/11 and SGS17/118/OHK1/2T/11, by the Czech Science Foundation research project 15-12420S. The authors would also like to thank to Tereza Horová for her help with this research.

References

1. L. Yan, R. L. Pendleton, C. H. M. Jenkins, "Interface morphologies in polyolefin fiber reinforced concrete composites," *Composites Part A.*, vol. 29A, pp. 643-650, 1998.
2. P. C. Tatnall, "Fiber-Reinforced Concrete," in *Significance of Tests and Properties of Concrete and Concrete-Making Materials*, J. F. Lamondband J. H. Pielert, Ed. West Conshohocken: Barr Harbor Drive, 2006, pp. 578-590.

3. J. Trejbal et al., "Interface enhancement between polymeric macro fibers and cement matrix by plasma treatment," in *Proceedings of the Nanocon 2016 8th international conference on nanomaterials – research and application*, Brno, Tanger, 2016, pp. 368-374.
4. P. Bílý et al. "Development of special fibre reinforced concrete for exposed concrete pavements on bridges," *Fibre Concrete 2015 - Technology, Design, Application*, vol. 2, pp. 8.
5. J. Trejbal et al., "Impact of surface plasma treatment on the performance of PET fiber reinforcement in cementitious composites," *Cement and Concrete Research*, vol. 89, pp. 276-287, 2016.
6. A. Tagnit-Hamou, Y. Vanhove, N. Petrov, *Cement and Concrete Research*, vol. 35, pp. 364-370, 2005.
7. V. Machovič et al., "Raman micro-spectroscopy mapping and microstructural and micromechanical study of interfacial transition zone in concrete reinforced by poly(ethylene terephthalate) fibres," *Ceramics and Silicates*, vol. 52, no. 1, pp. 54-60, 2008.
8. L. Kopecký et al., "Surface modification of PET to improve mechanical properties of cement composites," in *Proceedings of 33rd ICMA Conference*, San Francisco, International Cement Microscopy Association, 2011.
9. B. Wei, H. Cao, S. Song, "Tensile behaviour of contrast of basalt and glass fibers after chemical treatment," *Mater Des.*, vol. 31, no. 9, pp. 4244-4250, 2010.
10. S. E. Elsaka, "Influence of chemical surface treatments on adhesion of fiber posts to composite resin core materials," *Dent. Mater.*, vol. 29, no. 5, pp. 550-558, 2013.
11. V. Machovič et al., "Microstructure of interfacial transition zone between PET fibres and cement paste," *Acta Geodyn. Geomater.*, vol. 10, pp. 121-127, 2013.
12. Z. Lin, V. C. Li, "Crack bridging in fiber reinforced cementitious composites with slip-hardening interfaces," *J. Mech. Phys. Solids*, vol. 45, no. 5, pp. 763-787, 1997.

Proceedings of the Nanotech Middle East 2017 International Conference
Dubai, UAE – December 4 – 6, 2017
DOI: https://doi.org/10.26799/cp-nanotechme2017

The AFM and Raman Study of Few Layer Graphene

Narek Margaryan[1], Ninel Kokanyan[2,3], Edvard Kokanyan[4,5],
[1]National Polytechnic University of Armenia
Yerevan, Armenia, n.margaryan@polytechnic.am
[2]Université de Lorraine, Laboratoire Matériaux Optiques, Photonique et Systèmes,
Metz, F-57070, France
[3]Laboratoire Matériaux Optiques, Photonique et Systèmes, CentraleSupélec, Université Paris-Saclay,
Metz, F-57070, France
[4]Armenian State pedagogical University, Yerevan, Armenia
[5]Intitute for Physical Researches, National Academy of Sciences of Armenia, Ashtarak, Armenia

Abstract
In this paper, the synthesis process an characterizations of graphene layers are discussed. The Atomic force microscopy (AFM) and Raman spectroscopy is used to study surface and structural properties of obtained layers. Cross sectional and histogram analysis are used to describe obtained AFM images. The relationship between typical Raman peaks is discussed.

1. Introduction

Having huge application potential, graphene and related materials are under general attention. The process of forming the nanostructured graphene layers for modern electronic devices is accompanied by a process of self-organization at the nano and micro levels [1]. The geometric form of such self-organizing structures has the character of self-similarity. Since the resulting layers have only an atomic thicknesses and a very flat surface, it is very difficult to investigate their structural properties. Therefore, the best ways to study these nanofilms are atomic force microscopy and Raman spectroscopy.

2. Experiment and Investigation

Investigated graphene layers were obtained by complex method, which consists of two steps. At first, the method contains liquid phase exfoliation of highly oriented pyrolytic graphite powder. Then peeling graphene flakes because of their hydrophobic nature by combining together form whole layers. Thus, self-organized layers of graphene are obtained.

The AFM image of formed bilayer graphene sheet and corresponding cross sectional line scanning analysis are depicted in Fig. 1.

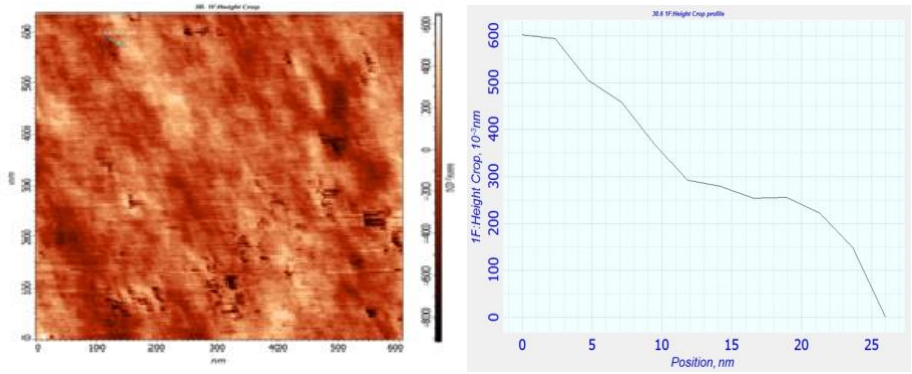

Fig. 1: AFM imag of film surface and corresponding linear scanning analysis.

The cross sectional analysis (Fig. 1) indicates two formed layers with 0.33 nm thiknesses. This values for thiknes are typical for epitaxial graphene [2]. As follows from Fig. 1, the surface of the film has some waveness, because of substrate roughness. Despite this, the surfaces of formed layers are comparatively smooth, and any granulated forms are absent. In addition, histograma for surface AFM image is studied to revelve the distribution of layer. In addition, histograma (Fig. 2) for surface AFM image is studied to examine the distribution of film thickness.

Proceedings of the Nanotech Middle East 2017 International Conference
Dubai, UAE – December 4 – 6, 2017
DOI: https://doi.org/10.26799/cp-nanotechme2017

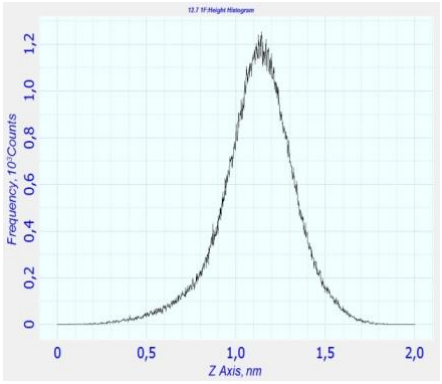

Fig. 2: Layer thickness distribution.

As follows, the peak of the distribution corresponds to approximately 1.2 nm. If we take the thickness of the graphene layer is about 0.33 nm, it can be assumed that the histogram corresponds to four layer graphene.
Of course, one of the main characteristics of graphene layers is the spectrum of Raman scattering [3, 4]. Obtained for few layer graphene, Raman spectrum is presented in Fig. 3. Corresponding to C-C bond, G peak is located at 1586 cm^{-1}.

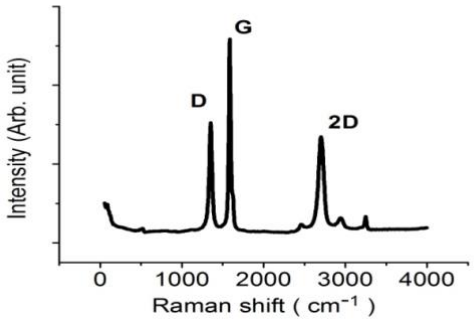

Fig. 2: Raman spectroscopy of few layer graphene.

The intensity of this peak exceeds by 1.89 times the intensity of 2D peak (corresponding to sp^2 carbon), which is at 2686 cm^{-1}. Because of their fractal essence, these graphene layers do not get rid of defects. Located at 1344 cm^{-1}, D peak describes the level of defects. The intensities of the three peaks are related to $I_D : I_G : I_{2D} = 59 : 100 : 54$ by the relationship.

3. Conclusion

Thus, self-organized graphene layers are formed from liquid phase exfoliated graphene flakes. As can be concluded from AFM images analysis, formed layers have smooth surface and thickness, typical for graphene. Raman spectroscopy confirms the presence of few layer graphene. In spite of their fractal character this layers have general properties of grapheme.

References

1. N. Margaryan, Investigation of the Surface Properties of Diamond-Like Carbon Films Using Multifractal Analysis. Journal of Physical Science and Application 7 (2) (2017) 46-51
2. H. Lu et al (2015) Synthesis of few-layer graphene by lamp ablation. CARBON 94: 349–351
3. H. Liu et al, Synthesis and characterization of graphene and carbon nanotubes: A review on the past and recent developments. Journal of Industrial and Engineering Chemistry 20 (2014): 1171–1185
4. Z. Ismail et al (2017) Application of graphene from exfoliation in kitchen mixer allows mechanical reinforcement of PVA/graphene film. Appl Nanosci 7:317–324

Proceedings of the Nanotech Middle East 2017 International Conference
Dubai, UAE – December 4 – 6, 2017
DOI: https://doi.org/10.26799/cp-nanotechme2017

Interaction Enhancement between Glass Micro-fibre Reinforcement and Cement and Lime-based Matrix

Jan Trejbal[1], Zdeněk Prošek[2]
[1]Czech Technical University in Prague, Faculty of Civil Engineering, Department of Mechanics, Thákurova 7, Prague, Czech Republic, EU, jan.trejbal@fsv.cvut.cz
[2]University Centre for Energy Efficient Buildings of Technical University in Prague, Třinecká 1024, Buštěhrad, Czech Republic, EU, zdenek.prosek@fsv.cvut.cz

Abstract
This work is focused on a bond and an adhesion improvement between glass fibres and lime-based and cement matrix by a plasma treatment. In order to improve surface properties of the glass fibres, we treated them by the cold low-pressure coupled oxygen plasma having a twofold modification effect – chemical (surface activation by active polar groups) and physical (surface roughening via ion bombardment). We examined chemical changes onto fibre surfaces by means of wettability measurements, while physical changes were assessed using SEM. The interaction between the two different matrixes and the treated fibres was tested indirectly by a four-point bending test of reinforced prismatic specimens, where their response during loading was observed and evaluated using DIC analysis. We found out that the wettability of the fibres significantly increased – almost two-times when treatment time exceed 2 minutes. However, as observed using SEM, the sizing of thus treated fibres was too much damaged after the mentioned time. Therefore, for purposes of this study, 60 seconds treated fibres were used as reinforcement of the cement paste and the lime-based mortar specimens (40×40×160 mm) which were subjected to four-point bending tests. These tests revealed that, despite of positive results from the previous experiments, the mechanical performance of specimens reinforced with treated fibres was worse, if compared to reference samples.

Keywords: glass fibres, fibre reinforcement, surface treatment, plasma, interface interaction, cement matrix, lime-based matrix, fibrous composites.

1. Introduction

Hydraulic lime as well as cement can be considered as the most used binder in the field of the civil engineering materials, concretely for production of mortars, concrete mixtures, etc. Hydration of both mentioned binders is accompanied by drying and shrinkage resulting on creation of crack and their following development [1-3]. This phenomenon has a strong impact on mechanical properties as well as lifetime and quality of materials in which the binder were used [4, 5]. These accompanying hydration phenomena can be reduced by several technological aspects – e.g. mixture treatment in early stages of the hydration (avoiding too rapid drying) or appropriate design of the mixture (water to binder ratio reduction, admixtures application), etc. [6, 7]. Unfortunately, these approaches do not guarantee satisfying results. Therefore, the utilization of a fibre reinforcement seems to be an effective possibility to control creation, development and width of cracks via crack bridging. Moreover, the reinforcement gives ductility to materials and ensures their integrity when load exceed maximal tensile strength stress [4, 5, 8, 9]. It has been shown, that one of the most effective reinforcement material type is glass. Glass fibres exhibit a very favourable ratio between cost and toughness or tensile strength, if compared to material alternatives like steel, polymer, plan-based, carbon, etc. Next to that, these fibres are very easy to be mixed into the mortars or the concrete due to their bulk density 2680 kg/m^3, which is not significantly different to other components of mixtures. For an overview: steel fibres have 7850 kg/m^3, common polymeric fibres about 1000 kg/m^3 [10]. Thanks to that, there is no segregation through the mixtures caused by sedimentation or, on the contrary, washing out of fibres.
Glass fibres are characterized by their geometric (length, diameter, shape), bulk (chemical composition, mechanical performance) and surface (reactivity to other material, roughness) properties. The third mentioned property is influenced by technology production, if made by a method of continuous casting. The glass filaments are highly abrasive to each other. Therefore, to avoid their self-destruction, fibre surfaces are treated by size coating. Moreover, composition of the sizing is designed to give to the fibre some other added protection like resistance to alkali environment, lubrication (for better homogenization with other phases within a composite material) and compatibility to other materials. Fibres made especially to be used as a reinforcement of materials in the civil engineeringare coated by water flushable or water resistance polymer-based (epoxide, urethane, polyester) sizing, whose thickness is in order to hundreds of nanometers

DOI: https://doi.org/10.26799/cp-nanotechme2017

[10]. Although, manufacturers adapt the sizing composition with regards to its interaction with matrixes of reinforced materials, not always strong bond and adhesion is ensured due to sizing chemical inertness (to water or lime or cement binders because of low surface free energy) and smooth surfaces.
In order to eliminate unfavourable surface properties of the sized glass fibres, an additional treatment should be done. As researched in many studies, there are known different surface treatments that can be divided into three groups as follows: wet (chemical modification using strong acid or alkali solutions, an electrochemical treatment), dry (plasma modification, gamma irradiation, high temperature) and as a marginal affair – multi-scale (growth of nanoparticles). It is also worth noting that the sizing application is in its essence ranked among wet non-oxidative modifications [11-14]. By a more detailed analysis of all of mentioned surface modifications, it can be concluded that this treatment can be described as non-ecological, long-lasting, ineffective and unconsiderate to fibres, eventually, mentioned drawbacks can be arbitrarily combined. However, as the exception, plasma treatment can be considered as effective from all point of views. This method videlicet combines a twofold effect – chemical as well as physical, if suitable type of plasma used. Via free radicals contained in the plasma, functional polar groups activate fibre surfaces – i.e. the surface free energy is thus increased. Consequently, the surface after the modification is highly reactive to water as a polar liquid (present in the mixtures always). The mentioned phenomenon ensures an estimation of the strong bond between the two materials. Above that, ion bombardment, known as a sputtering effect, roughen modified surfaces, so the surface area, where chemical bonds are realized, is increased a just like it, the mechanical interaction – adhesion – is thus enhanced too [15, 16]. One should bear in mind, that the sputtering effect must be applied properly to avoid complete removal of the sizing from fibres. An ideal situation occurs, when the sizing is slightly roughened on its surface, as imagined in the Fig. 1.
We treated the glass micro-fibres having 14 μm in the diameter and 12 mm in length, using the cold low-pressure oxygen plasma. The treatment time differed from 1 to 16 minutes. In order to reveal achieved changes after the modification, we observed fibre surfaces by SEM and subjected them to the water wettability measurement. The real interaction between fibres and two types of matrixes was established through destructive bending tests of prismatic specimens reinforced with the fibres.

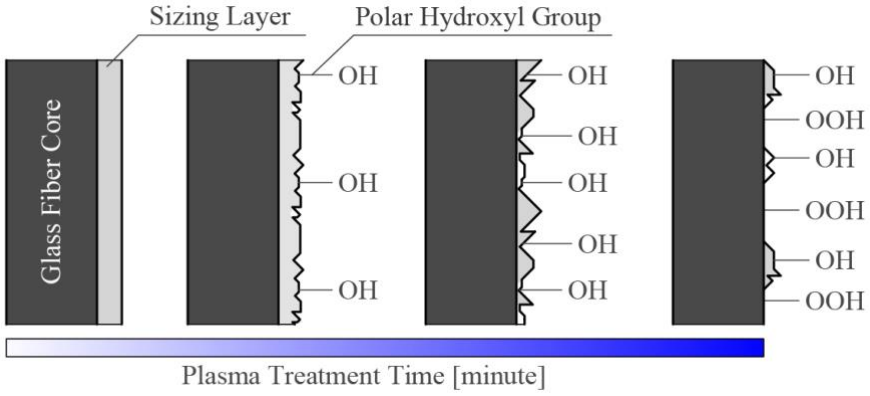

Fig. 1: A rate of damage of the sizing depending on plasma power or treatment time, from the left-hand side: original, ideally treated, maximally treated and too much treated fibre surface, inspired by: [14].

2. Materials

2.1. Matrixes

Two types of matrix, representing the most common matrixes in the field of civil engineering, were used – cement paste (w/c ratio equal to 0.4) and lime based mortar. Detailed mixtures composition is summarized in the Table 1, where LF_R and LF_P represent lime-based mixtures reinforced with reference and plasma treated fibres, respectively and CF_R and CF_P indicate the cement matrixes with the same logic of the fibre type marking. The lime-based mortar samples were stored in standard laboratory conditions, while the cement ones were submerged into water, both for 28 days.

Table 1: Composition of mixtures.

Mixture	Lime CL-90	Metakaoline Mefisto L 0.5	Cement CEM I 42.5 R	Sand ST2 and STJ25	Water	Fibres
	wt. %					
LF_R/P	14	5	-	57	22	2

DOI: https://doi.org/10.26799/cp-nanotechme2017

CF_R/P	-	-	77	-	21	2

2.2. Fibres
For purposes of this study, we used glass fibres, which are determined for reinforcing silicate matrixes like concrete, and mortars. The fibres properties are as follows: the tensile strength 3500 MPa, the Young's modulus of elasticity 72 GPa, the density 2680 kg/m^3, the elongation 2.4 %, the diameter 14 μm, the length 12 mm, the sizing: irremovable (no more information about the sizing was provided by their manufacturer).

3. Methods

3.2. Plasma Treatment
To improve the water wettability of fibres and to roughen their surface, an oxygen treatment in inductively coupled plasma system (VT 214, Tesla) was done. Plasma treatment parameters were as follows: the total power 100 W, the total gas pressure 60 Pa, the 50 sccm O2 flow, and the exposition time differed from 1 to 16 minutes.

3.2. Contact Angle Measurements
A direct horizontal optical method was used for fibre wettability evaluation, according to [17]. The each single fibre was perpendicularly submerged into demineralized water, while the meniscus of the liquid adhering around fibres were captured and then evaluated using MatLab based SW CAMTIA [18]. The final contact angle value was averaged from 6 independent measurements.

3.3. SEM Morphology Analysis
To assess the rate of the fibre surface roughening, the scanning electron microscope (Zeiss Merlin, Carl Zeiss Microscopy GmbH) was used for fibre morphology analysis. To eliminate surface charging, a golden layer about 10 nm thick was applied onto fibres (by BOC Edward Scancoats Six), as reported in our previous work [15].

3.4. Bending Tests
The chemical as well as the mechanical interaction between the fibres and the matrix (both cement and lime-based, separately) was examined via mechanical bending tests. We were based on the assumption, that the more chemical bond between the two materials, the more initial bending toughness of tested specimens. Just like that, the more physical interaction between them, the more post-cracking toughness of specimens. After mixtures curing and hardening, the testing was carried out using the loading frame Heckert FP 100. The bending tests were displacement-controlled at the constant rate of 0.3 mm/min. Dimensions of specimens were equal to 40×40×160 mm. Load-displacement dependence of each mixture was averaged from 6 independent measurements.

3.5. DIC Analysis
During the specimens loading, the behaviour of cracks was observed using digital image analysis (DIC). The DIC analysis allowed to image the amount, the shape and the position of cracks graphically and thus to answer the question how specimens resisted to loading in the post-cracking phase, as reported in [19]. As the result of the analysis, cracking patterns were visualized with a map of a maximum principal strain in which concentrations can be attributed the crack formation.
To allow the DIC observation, the samples were equipped with an artificial stochastic contrast pattern onto their surfaces. Images used for DIC analysis were taken with DSLR camera Canon EOS 70D fitted with Canon zoom lens EF-S 17-85 IS USM. The exposition parameters were as follows: the shooting interval 10 seconds, the ISO speed 100, the focal length 50 mm, the aperture value 4.5, the shutter speed 1/100 sec.

4. Results

4.1. Contact Angle Measurements

It was found out, that the wettability of the fibres by demineralized water was increased significantly after the plasma treatment, as Fig. 2 illustratively shows, where the most representative pictures, corresponding to the certain treatment time, are pictured. The contact angle measured on the reference fibres is equal to 78.3±9°, while angles detected after the modification were 70.1±7°, 43.5±7°, 39.6±8° and 32.6±9° for treatment times 1, 2, 8 and 16 minutes, respectively. As it seems from the Fig. 3, the most rapid wettability change was achieved during the first 2 minutes of the treatment. After that, as the treatment increased, the wettability slightly linearly increased. It should be added, that the accuracy of the measurement is limited because of fibres small diameter and light transparency. Based on these findings, it seems to be appropriate to use the fibres modified by 2 minutes for following experiments but with respect to the physical surface modification, this treatment duration is too much long, as explained below.

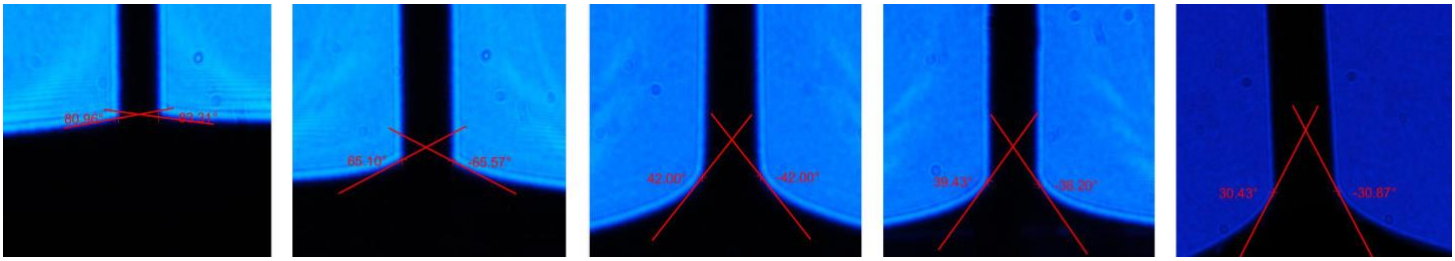

Fig. 2: Digital camera photos of the fibres submerged into water captured during the wettability test, from the left-hand side: reference, 1, 2, 8 and 16 minutes plasma treated, respectively.

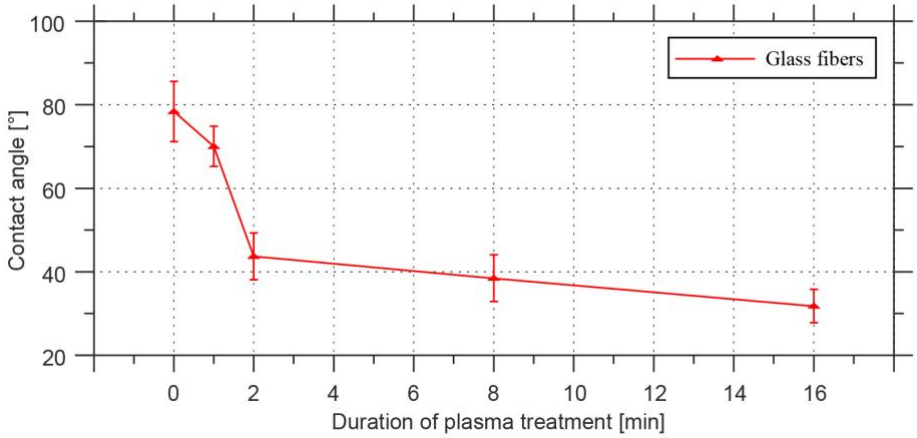

Fig. 3: Contact angle values as a function of plasma treatment duration.

4.2. SEM Morphology Analysis

The SEM revealed that surfaces of the reference fibres are rugged due to presence of the sizing – see Fig. 4 in which the most representative pictures belonging to the specific treatment time are shown. According to the idea mentioned earlier and imagined in the Fig. 1, to achieve required changes onto fibre surfaces – slight roughening – the most convenient is the treatment duration lasting for 1 minute. If this time is exceeded, the sizing is completely removed from fibre surfaces. Thus exposed fibres can be easily damaged by sharp edges of the aggregate during mixture preparation. The picture belonging to 8 minutes of the treatment represents all of the surface changes created between 2 and 16 minutes of the treatment duration.

4.3. Bending Tests

The results of experiments stayed far beyond our expectation for both mixture types. Fig. 5 shows the dependence between the load and the displacement of lime-based mortar samples. It was shown that both, the initial toughness and the load-bearing capacity were higher in the case of samples reinforced with reference fibres (LF_R). While the LF_R mixture reached almost to 1.5 kN, the LF_P only to ca. 0.6. The only possible cause of this result is weakening of the

DOI: https://doi.org/10.26799/cp-nanotechme2017

sizing layer, as a result, the fibres were damaged by grains of the sand. Moreover, for both mixtures, post-cracking behaviour is common. There is obvious softening referencing to the single crack opening.

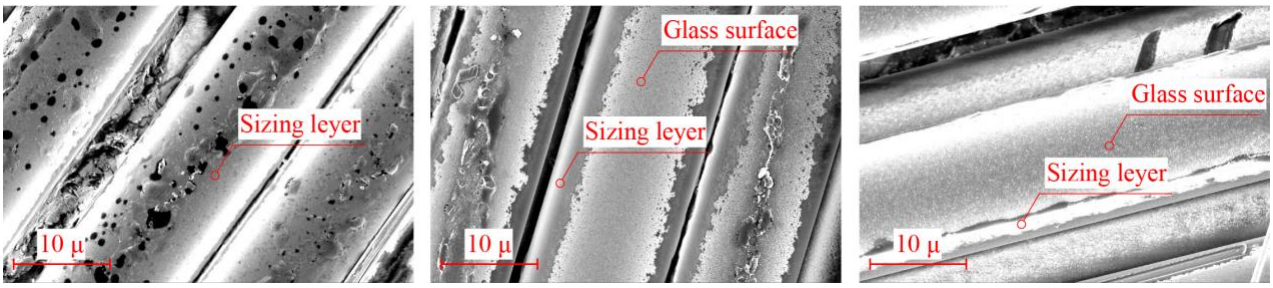

Fig. 4: SEM image of reference (left) and plasma treated (1 min – centre, 8 min – right) fibres.

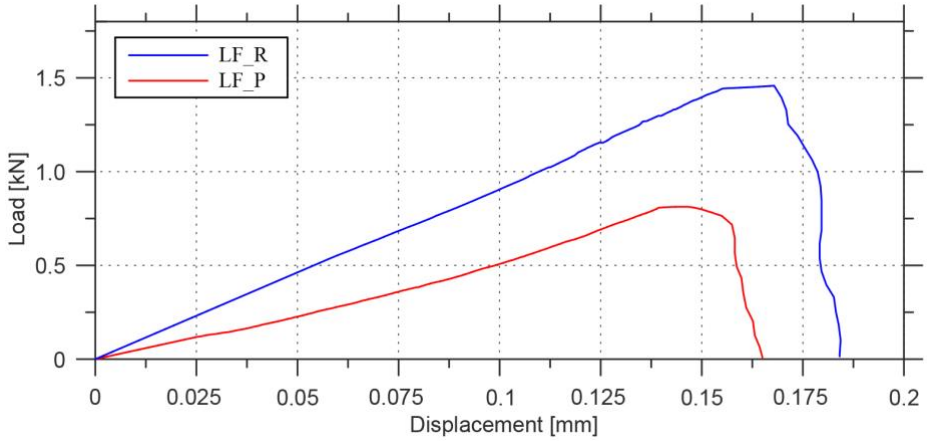

Fig. 5: Load-displacement diagrams of lime-based mortar reinforced with the glass fibres.

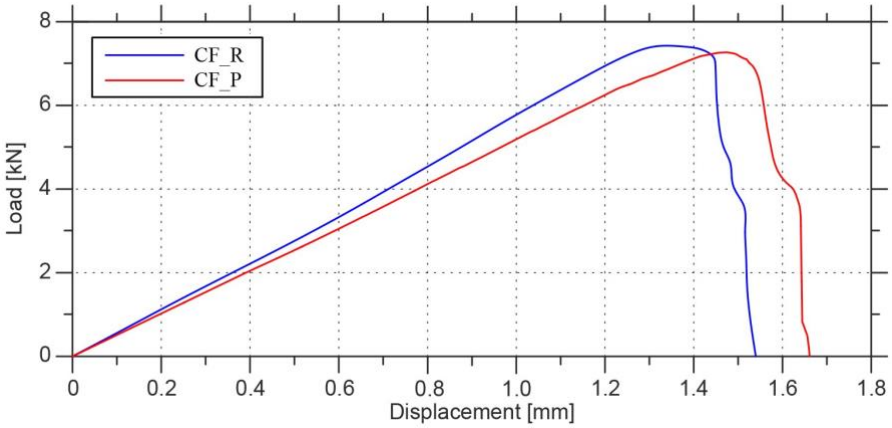

Fig. 6: Load-displacement diagrams of lime-based mortar reinforced with the glass fibres.

As in the case of lime-based mortar samples, cement samples mechanical behaviour turned out worse, than we expected. As captured in The Fig. 6, there is no difference between samples CF_R (containing reference fibres) and CF_P (plasma treated fibres). Both, the initial toughness as well as the load-bearing capacity, stayed unchanged regardless to the fibres treatment. Commonly, for the CF_R and CF_P, the post-cracking response corresponds to single-crack opening, which is characteristic to brittle samples, not fibre reinforced.

4.4. DIC Analysis

For all of the tested specimens (LF_R, LF_P, CF_R, CF_P) the DIC analysis showed that when the load-bearing capacity was reached, each sample was broken by a single crack. The crack was quickly opened with an increased displacement. It was not achieved of the multi-crack behaviour, so the crack bridging was insufficient. According to our explanation,

DOI: https://doi.org/10.26799/cp-nanotechme2017

these phenomenon can originated into two opinions: (i) the adhesion between the fibres and the matrix was too poor, or (ii) the amount of the fibres was too small.

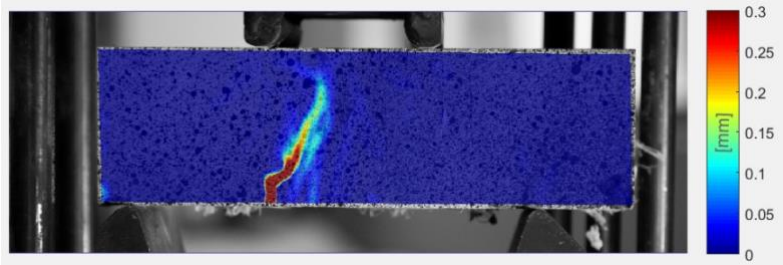

Fig. 7: Crack development during four-point bending test of cement sample reinforced with the glass fibres.

5. Conclusion

We treated industrial sized (by water insoluble sizing) glass micro fibres having 14 μm in a diameter in order to change their surface properties from hydrophobic to hydrophilic and from smooth to roughened and thus to ensure strong interaction between the fibres and the two types of often used matrixes in the field of civil engineering – lime-based and cement. To attain the target changed, we used the cold low-pressure oxygen plasma treatment. We controlled an intensity of the plasma by different treatment times (from 1 to 16 minutes), where we focused on its influence on fibre surfaces.
After the modification, chemical changes caused by surface activation via active polar groups on the fibre surfaces was researched using a wettability measurement, when the fibres were wetted by demineralized water and the interface between the two materials (in the presence of the third phase – air) was observed and evaluated. Physical changes caused via ion bombardment were assessed by means of the SEM image analysis. The real interaction between the fibres and the matrixes was evaluated by means of a bending tests, when the specimens having dimensions equal to 40×40×160 mm were made from special designed mixtures representing both, the lime-based and the cement binders. Both types of mixtures were reinforced with reference and treated fibres in amount corresponding to 2 % of sample weight. Response of samples was monitored during the loading. We focused on the dependence between the load and the displacement as an indicator of samples responses. Moreover, we observed loaded samples using DIC technique in order to reveal the creation and the development of cracks in the post-cracking phase.
We found out that the fibre wettability increased after the plasma modification – during the first 1 minute slightly (only by ca. 10 %). The significant wettability improvement occurred after 2 minutes of the treatment, when ca. 45% increase was detected. The longer-lasting treatment did not bring any other significant wettability changes. Compared to that, legible morphology changes on fibre surfaces were detected by means of the SEM already after 1 minute of the modification. When the treatment time exceed 1 minute, the fibre surfaces were damaged too much (the sizing was completely removed). Contrary to our expectations, bending tests pointed out to the deterioration of the adhesion between the fibres and the matrix. In the case of the lime-based matrix, samples reinforced with treated fibres did not reached to load-bearing capacity of reference samples. In the case of the cement matrix, if we compare samples containing treated fibres to reference ones, there were no detected changes in the mechanical response during the testing. All of the tested samples were damaged by one single crack, as proven by the DIC analysis. Based on our findings, it can be concluded, that it is not favourable to modify glass fibres via plasma for purposes of the reinforcement of silica-based matrixes.

Acknowledgements
This work was financially supported by Czech Technical University in Prague – SGS project SGS16/201/OHK1/3T/11, by the Czech Science Foundation research project 15-12420S and by the Ministry of Education, Youth and Sports within National Sustainability Programme I, project No. LO1605. The authors would also like to thank to Tereza Horová for her help with this research.

References
1. J. Bisschop and J. G. M. van Mier, "Drying shrinkage microcracking in cement-based materials," *Heron*, vol. 47, no. 3, pp. 163-184, 2002.
2. T. Ayano and F. H. Wittman, "Drying, moisture distribution, and shrinkage of cement-based materials," *Materials and Structures*, vol. 35, pp. 134-140, 2002.

3. L. Svoboda et al., *Stavební hmoty 2*, Bratislava, Jaga Group, 2013.
4. M. di Prisco, G. Plizzari, and L. Vandewalle, "Fibre reinforced concrete: new design perspectives," *Materials and Structures*, vol. 42, no. 9, pp. 1261-1281, 2009.
5. P. C. Tatnall, "Fiber-Reinforced Concrete," in *Significance of Tests and Properties of Concrete and Concrete-Making Materials*, J. F. Lamondband J. H. Pielert, Ed. West Conshohocken: Barr Harbor Drive, 2006, pp. 578-590.
6. D. P. Bentza, M. R. Geikerb and K. K. Hansenb, "Shrinkage-reducing admixtures and early-age desiccation in cement pastes and mortars," *Cement and Concrete Research*, vol. 31, no. 7, pp. 1075-1085, 2001.
7. A. A. Melo, et al., "Drying and autogenous shrinkage of pastes and mortars with activated slag cement," *Cement and Concrete Research*, vol. 38, no. 4, pp. 565-574, 2008.
8. A. Naaman and H. Reinhardt, "High performance fiber reinforced cement composites: Classification and applications," *Materials and Structures*, vol. 36, pp. 389-401, 2003.
9. F. Iucolano, B. Liguori, and B. Colella, "Fibre-reinforced lime-based mortars: A possible resource for ancient masonry restoration," *Construction and Building Materials*, vol. 38, pp. 785-789, 2003
10. F. T. Wallenberger et al., "Glass fibers," in *ASM Handbook Volume 21: Composites*, D. B. Miracle and S. L. Donaldson, Ed. Ohio, 2001, pp. 27-31.
11. V. Cech et al., "Enhanced interfacial adhesion of glass fibers by tetravinylsilane plasma modification," *Composites: Part A*, vol. 58, pp. 84-89, 2014.
12. D. Cökeliler et al., Modification of glass fibers to improve reinforcement: "A plasma polymerization technique," *Dental Materials*, vol. 23, pp. 335-342, 2007.
13. B. Wei, H. Cao and S. Song, "Tensile behaviour contrast of basalt and glass fibers after chemical treatment," *Materials and Design*, vol. 31, pp. 4244-4250, 2010.
14. M. Sharma et al., "Carbon fiber surfaces and composite interphases," *Composites Science and Technology*, vol. 102, pp. 35-50, 2014.
15. J. Trejbal et al., "Wettability enhancement of polymeric and glass microfiber reinforcement by plasma treatment," in *Proceedings of the Nanocon 2015 7th international conference on nanomaterials – research and application*, Brno, Tanger, 2015, pp. 315-320.
16. J. Trejbal et al., "Impact of surface plasma treatment on the performance of PET fiber reinforcement in cementitious composites," *Cement and Concrete Research*, vol. 89, pp. 276-287, 2016.
17. J. Trejbal et al. "Direct optical method for contact angle measurement on micro fibers," in *Proceedings of the Nanomaterials and nanotechnology in civil engineering 2015*, Prague, CTU in Prague, 2015, pp. 89-90.
18. V. Nežerka, M. Somr and J. Trejbal. (2017, Nov 19). Contact angle measurement tool based on image analysis. [Online]. Available: http://mech.fsv.cvut.cz/~nezerka/software.html
19. B. Pan et al., "Full-field strain measurement using a two-dimensional Savitzky-Golay digital differentiator in digital image correlation," *Optical Engineering*, vol. 46, pp. 1-10, 2007.

Proceedings of the Nanotech Middle East 2017 International Conference
Dubai, UAE – December 4 – 6, 2017
DOI: https://doi.org/10.26799/cp-nanotechme2017

A hidden correlation between absorption spectra of graphene nanoribbons and carbon nanotubes

Vasil Saroka[1], Mikhail Shuba[1] and Mikhail Portnoi[2]

[1]Institute for Nuclear Problems, Belarusian State University
Bobruiskaya 11, 220030, Minsk, Belarus, .40.ovasil@gmail.com
[2]School of Physics, University of Exeter
Stocker Road, EX4 4QL, Exeter, United Kingdom

Abstract
In this paper, we study optical absorption in zigzag graphene nanoribbons and armchair carbon nanotubes. Within the orthogonal tight-binding model with the nearest neighbour approximation, it is shown that if the ribbon width is about a half of the tube circumference then there is a correlation between all but the first absorption peaks in the tubes and those absorption peaks in the ribbons that do not originate from the edge states. Knowledge about this correlation effect should be useful in designing ribbon- and tube-based optoelectronics devices without a crosstalk.

Keywords
carbon nanotubes, graphene nanoribbons, optical matrix elements, optical absorption, selection rules

1. Introduction
Graphene nanoribbons and carbon nanotubes are both quasi-one-dimenstional structures based on graphene – a monolayer of carbon atoms arranged into a honeycomb lattice. Depending on the geometry of their edges (for ribbons) or terminations (for tubes) they can be classified on two major types – zigzag and armchair. Such classification ensures that zigzag carbon nanotube unrolls into an armchair graphene nanoribbon, while an armchair carbon nanotube unrolls into a zigzag graphene nanoribbon. This transformation, preserving the number of atoms in the unit cells of both structures, is naturally expected to preserve their properties. Indeed, a similarity has been mentioned in a number of papers based on the tight-binding models [1–4]. However, an alternative approach to matching properties of the tubes and ribbons is also possible. For instance, one may choose to match transverse electron momenta quantized by the periodic (in tubes) and hard wall (in ribbons) boundary conditions. It has been shown that the matching of the transverse momenta leads to a perfect match of the energy band structures of the armchair graphene nanoribbons and zigzag carbon nanotubes [5]. A similar observation has been reported for zigzag graphene nanoribbons and armchair carbon nanotubes [3]. However, optical properties are beyond the scope of these studies. At the same time, the majority of the literature on the optical properties of tubes and ribbons mostly highlights differences between the two types of structures: selection rules, presence of the edge states and edge to bulk state transitions. Nevertheless a recent theoretical analysis of the optical matrix elements revealed that equivalence between armchair tubes and zigzag ribbons should also extend to their optical properties even if the curvature and edge effects are taken into account [6]. Similar analysis of the matrix elements has been carried out for zigzag ribbons and armchair tubes in Refs. [7,8].

In this paper, we focus on the optical absorption spectra of zigzag graphene nanoribbons and armchair carbon nanotubes. We show within the orthogonal tight-binding model with the nearest neighbour approximation that if transverse electron momenta are matched for both structures then a correlation takes place between optical absorption peaks of zigzag graphene nanoribbons (ZGNRs) and armchair carbon nanotubes (ACNTs).

2. Results and Discussion
Hereafter we follow a standard description of the carbon tubes in which a pair of indices (n, m) describes the chiral vector specifying the crystallographic orientation along which the graphene rolling

DOI: https://doi.org/10.26799/cp-nanotechme2017

is performed to obtain the tube. Thus, we refer to an armchair carbon nanotube as ACNT(n,n). For zigzag graphene nanoribbon description, we introduce a width index, w, equal to the number of carbon atom pairs in the ribbon unit cell. Thence, a specific zigzag graphene nanoribbon is referred to as ZGNR(w). In Fig. 1, we show that the energy band structures (E/γ, where γ is the hopping integral) of ZGNRs and ACNTs can be approximately matched either at the edge or centre of the Brillouin zone [9]. This is different to what is observed for armchair graphene nanoribbons and zigzag carbon nanotubes [5] and it can be attributed to that fact that the secular equation quantizing transverse electron momentum in zigzag ribbons depends on the electron longitudinal momentum [10]. If a number of atoms in the tube unit cell, N_t, is related to a number of atoms in the ribbon unit cell, N_r, as $N_t = 2N_r$ then the band structures follow a similar pattern at the edge of the Brillouin zone [see Fig. 1 (a)]. At same time, the energy band structures can be approximately matched at the centre of the Brillouin zone if $N_t = 2N_r + 4$ [see Fig. 1 (b)].

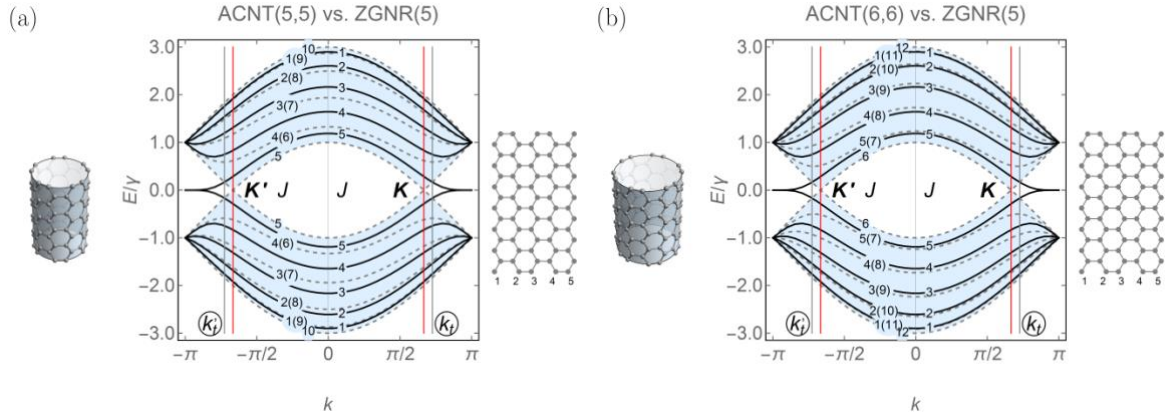

Fig. 1: The energy band structures of ZGNR (solid black) and ACNT (dashed grey) matched at the (a) edge and (b) centre of the Brillouin zone. The atomic structures of the corresponding tubes and ribbons are presented on both sides of the plots. The band enumeration is shown by J index. The double degenerate tube bands are labelled with two numbers, one of which is placed in parentheses. The vertical red lines mark positions of the graphene Dirac points (points **K** and **K'**), while vertical grey lines mark positions of the transition points k_t and k_t' which separates the edge and the bulk states in the ribbon band structure. The light blue area denotes the region of the graphene band structure.

In Fig. 2 we compare absorption spectra of ZGNR(w) of different widths with the spectra of ACNT(w,w) and ACNT$(w+1,w+1)$, for which the two above mentioned relations between N_t and N_r are fulfilled, respectively. As one can see, all but the lowest absorption peaks in ACNT$(w+1,w+1)$ spectrum have a pair peak in the absorption spectrum of ZGNR(w). The peaks in ZGNR(w) spectrum, which do not have a counterpart in the tube spectrum originate from the transitions involving the edge states. These edge states are seen in Fig. 1 as the bands escaping outside the light blue region. The correlated peak positions follow the simple analytical formula:

$$\omega_j = 2\gamma \sin\left(\frac{\pi j}{w+1}\right) \tag{1}$$

where $\gamma \approx 3$ eV is the hopping integral and $j = 2 \ldots w/2$ (w is even) or $(w-1)/2$ (w is odd). It is also seen that for wider ribbons, the number of the correlated peaks increases while they shift towards lower frequencies. Thus, for wide enough ribbons this correlation should take place in the visible range. One can also notice that the correlation occurs provided that there is more than one correlated peaks in the frequency range $\omega < 2\,\gamma$ for the given tube and ribbon. This condition is met for all the ribbons with $w > 5$. For ZGNR(5), however, there is only one correlated peak satisfying this condition, because correlation between the peak at $\omega = \gamma$ seen in Fig. 2 (a) and the lowest absorption peak in ACNT(6,6) is accidental as follows from the panels (b), (c) and (d) of Fig 2.

Proceedings of the Nanotech Middle East 2017 International Conference
Dubai, UAE – December 4 – 6, 2017
DOI: https://doi.org/10.26799/cp-nanotechme2017

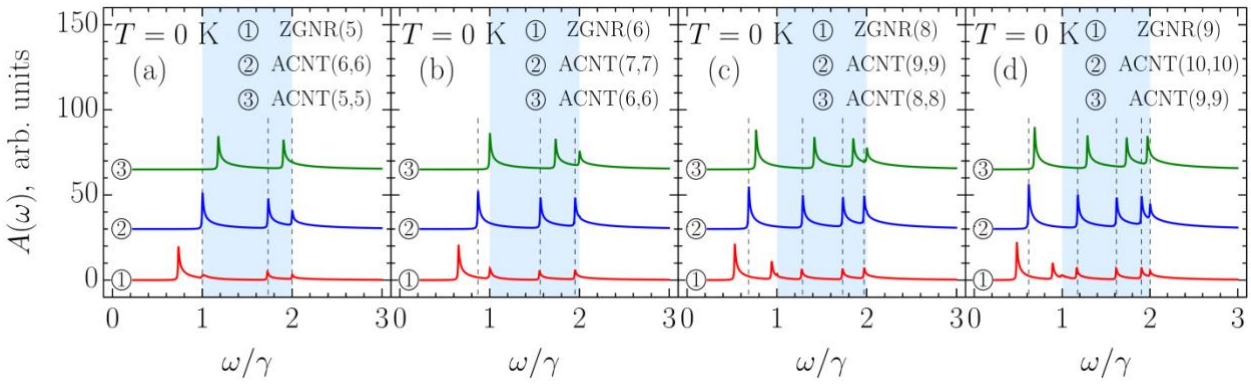

Fig. 2: The optical absorption spectra of zigzag graphene nanoribbons and armchair carbon nanotubes.

The correlation between the absorption peaks of ACNT$(w+1, w+1)$ and ZGNR(w) unveiled in Fig. 2 is a non-trivial effect. Note that neither energy levels nor selection rules for the two types of the chosen structures are the same [7]. Therefore, the effect can be dubbed as a hidden correlation. This hidden correlation implies that an armchair carbon nanotube can be decomposed onto two zigzag ribbons with optical properties very similar to those of the initial tube. Such decomposition is explicitly presented in Fig. 3. It is readily seen from Fig. 3 that $N_t = 2N_r + 4$ relation between the number of atoms in the tube and ribbon unit cells corresponds to the width of the ribbon, W, being a half of the circumference of the tube, C.

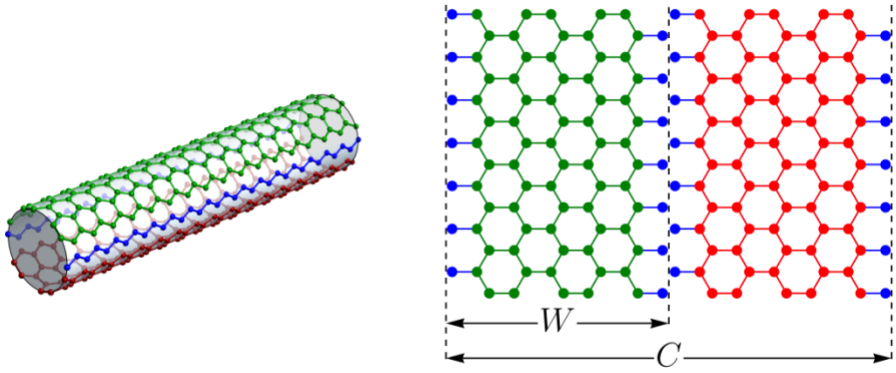

Fig. 3: The decomposition of ACNT$(6,6)$ onto two ZGNR(5) with optical properties that are equivalent to the initial tube: (a) 3D and (b) 2D model. The atoms coloured in blue should be removed from the structures.

3. Conclusion

In summary, we have shown that matching transverse momenta of the electrons in armchair carbon nanotubes and zigzag graphene nanoribbons allows one to "decompose" the tube onto two zigzag ribbons of equal width preserving positions of the optical absorption peaks of the initial tube. The correlation between peak positions of thus related tubes and ribbons should be important in optoelectronics applications either for enhanced resonance interaction between the structures or for avoiding a crosstalk in complicated devices. This ribbon-width- and edge-geometry-sensitive effect should be practical for optoelectronics applications since the methods of graphene nanoribbon synthesis are developing fast making high quality samples of ribbons more available for experimental studies [11]. For instance, recently graphene ribbons with zigzag edge topology have been produced by self-assembling technique with an ultimate edge quality [12]. At the same time, the carbon nanotube samples have also been drastically improved in quality. Along with the gradual advancement of the carbon nanotubes sorting techniques [13], the first successful attempt of their synthesis with pre-defined chirality has been reported [14]. Finally, we point out that the reported here correlation of

DOI: https://doi.org/10.26799/cp-nanotechme2017

the optical absorption spectra might also take place for tubes and superlattices based on graphene nanoribbons [15–18].

Acknowledgements

This work was supported by the EU FP7 ITN NOTEDEV (Grant No. FP7-607521), EU H2020 RISE project CoExAN (Grant No. H2020-644076), FP7 IRSES projects CANTOR (Grant No. FP7-612285), QOCaN (Grant No. FP7-316432), InterNoM (Grant No. FP7-612624), and Graphene Flagship (Grant No. 604391).

References

1. H. Hsu and L. E. Reichl, "Selection rule for the optical absorption of graphene nanoribbons," *Phys. Rev. B*, vol. 76, 045418, 2007.
2. K.-I. Sasaki, M. Yamamoto, S. Murakami, R. Saito, M. S. Dresselhaus, K. Takai, T. Mori, T. Enoki, and K. Wakabayashi, "Kohn anomalies in graphene nanoribbons," *Phys. Rev. B*, vol. 80, 155450, 2009.
3. L. I. Malysheva and A. I. Onipko, "Quantum conductance of achiral graphene ribbons and carbon tubes,"*J. Exp. Theor. Phys.*, vol. 108, no. 1, pp. 126-131, 2009.
4. A. Onipko, "Spectrum of π electrons in graphene as an alternant macromolecule and its specific features in quantum conductance," *Phys. Rev. B*, vol. 78, 245412, 2008.
5. C. T. White, J. Li, D. Gunlycke, and J. W. Mintmire, "Hidden one-electron interactions in carbon nanotubes revealed in graphene nanostrips," *Nano Lett.*, vol. 7, no. 3, pp. 825-830, 2007.
6. M. E. Portnoi, V. A. Saroka, R. R. Hartmann, and O. V. Kibis, "Terahertz Applications of Carbon Nanotubes and Graphene Nanoribbons," in *2015 IEEE Comput. Soc. Annu. Symp. VLSI*, Los Alamitos, CA, 2015, pp. 456–459.
7. V. A. Saroka, M. V. Shuba, and M. E. Portnoi, "Optical selection rules of zigzag graphene nanoribbons," *Phys. Rev. B*, vol. 95, 155438, 2017.
8. V. A. Saroka, M. V. Shuba, and M. E. Portnoi, "Erratum: Optical selection rules of zigzag graphene nanoribbons [Phys. Rev. B 95 , 155438 (2017)]," *Phys. Rev. B*, vol. 96, 199901, 2017.
9. V. Saroka, (2017, September 8). "Band Structures In Zigzag Graphene Nanoribbons And Armchair Carbon Nanotubes," Wolfram Demonstrations Project [Online]. Available: http://demonstrations.wolfram.com/BandStructuresInZigzagGrapheneNanoribbonsAndArmchairCarbonNa/.
10. V. Saroka, (2017, June 27). "Solving the Secular Equation for Zigzag and Bearded Graphene Nanoribbons," Wolfram Demonstrations Project [Online]. Available: http://demonstrations.wolfram.com/SolvingTheSecularEquationForZigzagAndBeardedGrapheneNanoribb/.
11. A. Celis, M. N. Nair, A. Taleb-Ibrahimi, E. H. Conrad, C. Berger, W. A. de Heer, and A. Tejeda, J. "Graphene nanoribbons: fabrication, properties and devices," Phys. D. Appl. Phys., vol. 49, 143001, 2016.
12. P. Ruffieux, S. Wang, B. Yang, C. Sánchez-Sánchez, J. Liu, T. Dienel, L. Talirz, P. Shinde, C. A. Pignedoli, D. Passerone, T. Dumslaff, X. Feng, K. Müllen, and R. Fasel, "On-surface synthesis of graphene nanoribbons with zigzag edge topology," *Nature*, vol. 531, no. 7595, pp. 489-492, 2016.
13. X. Wei, T. Tanaka, Y. Yomogida, N. Sato, R. Saito, and H. Kataura, "Experimental determination of excitonic band structures of single-walled carbon nanotubes using circular dichroism spectra," *Nat. Commun.*, vol. 7, 12899, 2016.
14. J. R. Sanchez-Valencia, T. Dienel, O. Gröning, I. Shorubalko, A. Mueller, M. Jansen, K. Amsharov, P. Ruffieux, and R. Fasel, "Controlled synthesis of single-chirality carbon nanotubes," *Nature*, vol. 512, no. 7512, pp. 61-64, 2014.
15. V. A. Saroka, K. G. Batrakov, and L. A. Chernozatonskii, "Edge-modified zigzag-shaped graphene nanoribbons: Structure and electronic properties," *Phys. Solid State*, vol. 56, no. 10, pp. 2135-2145, 2014.
16. V. A. Saroka, K. G. Batrakov, V. A. Demin, and L. A. Chernozatonskii, "Band gaps in jagged and

DOI: https://doi.org/10.26799/cp-nanotechme2017

straight graphene nanoribbons tunable by an external electric field," *J. Phys.: Condens. Matter*, vol. 27, 145305, 2015.

17. V. A. Saroka and K. G. Batrakov, "Dirac electrons of graphene nanoribbons tunable by transverse electric field," in *Physics, Chemistry and Applications of Nanostructures: Proceedings of International Conference Nanomeeting – 2015*, World Scientific, 2015, pp. 240–243.
18. V. A. Saroka and K. G. Batrakov, "Zigzag-Shaped Superlattices on the Basis of Graphene Nanoribbons: Structure and Electronic Properties," *Russ. Phys. J.*, vol. 59, no. 5, pp. 633-639, 2016.

Proceedings of the Nanotech Middle East 2017 International Conference
Dubai, UAE – December 4 – 6, 2017
DOI: https://doi.org/10.26799/cp-nanotechme2017

Ultrasound Assisted Oxidation of *p*-nitroaniline by Synthesized Ferroferric Oxide Encapulated Guaran Nanocomposite

J. Balachandramohan, M. Midhun Kumar, T. Sivasankar*

Department of Chemical Engineering, National Institute of Technology Tiruchirappalli, INDIA
*ssankar@nitt.edu

Abstract

Ferroferric oxide encapsulated guaran nanocomposites can be effectively used as a catalyst for the degradation of recalcitrant organic contaminants in wastewater. This catalyst was prepared through a simple ultrasound assisted liquid-phase co-precipitation method and were characterized using X-ray diffractometry, field emission scanning electron microscopy and high-resolution transmission electron microscope for their crystal structure, size and morphology of the core/shell catalyst. The sonochemical process or ultrasound treatment process has been an attractive and effective one due to its several beneficial factors when compared to other advanced oxidation processes. This ultrasound process when applied involves the formation, growth and collapse of transient cavitation bubbles. During this process temperature and pressure of higher degrees would be generated as per Hot Spot Theory leading to production of highly reactive hydroxyl and hydrogen radicals. The radicals were utilized for the oxidation of the treatment of pollutants. In this study highly, toxic *p*-nitroaniline was treated by sonochemical oxidation process and further exceptional improvement was achieved by the addition of sodium periodate. The *p*-nitroaniline is an organic non-biodegradable compound used as an intermediate or precursor in the manufacture of organic synthesis such as azo dyes, antioxidants, fuel additives, corrosion inhibitors, pesticides, antiseptic agents and the synthesis of pharmaceuticals. The effect of experimental parameters such as initial solution pH, catalyst dose, *p*-nitroaniline concentration and sodium periodate concentration were varied and their effect of the degree of treatment were studied and reported. The treatment efficiency of 94% in 120min. of reaction time was achieved at optimized condition. A feasible reaction mechanism for the degradation of *p*-nitroaniline was presented.

Keywords: Ferroferric oxide, Guaran, Ultrasound, *p*-nitroaniline, catalytic oxidation

1. Introduction

Aromatic amines are extensively used in biology and chemical industry. Exceptionally aniline and its derivatives are being used as antioxidants, and in production of dyes and pesticides [1, 2]. The aromatic amines are also used as intermediate in the synthesis of several pharmaceutical drugs including acetaminophen, nadifloxacin, difloxacin, sarafloxacin, flumequin, cisapride, bicalutamide, brequinar, sorbinil etc. [3]. Some of the para (p) substituted anilines have local anesthetic property, wherein amino group plays an important role in the interaction with respective receptor. *p*-nitroaniline (PNA) is an organic non-biodegradable compound used as an intermediate or precursor in the manufacture of organic synthesis such as azo dyes, antioxidants, fuel additives, corrosion inhibitors, pesticides, antiseptic agents, medicines for poultry and the synthesis of pharmaceuticals. Nevertheless, the chemical stability and toxicity of PNA in water, even at a low concentration, is extremely harmful to aquatic microorganism and human health in terms of its hematoxicity, splenotoxicity and nephrotoxicity [4] with a TLV (Threshold Limit Value) of 0.001kgm^{-3} comparatively lower than aniline 0.002kgm^{-3} [5-8]. The National Environmental Protection Agency (NEPA) of the People's Republic of China has been enlisted PNA as one of the priority contaminant in water [7].

Different treatment methods have been adopted for PNA removal from aqueous solution, ie., physical, chemical and biological methods [9-11], which includes hydrothermal decomposition [12], Fenton oxidation [13], photocatalytic degradation [14], biodegradation [15], adsorption [16–18] and others [8, 19]. The physical method of degradation of PNA such as carbon fiber [20] and carboxylated polymeric matrix absorptions [21], the mineralization could not be achieved, the pollutant changes from one form to another and further treatment was required. The chemical method,

DOI: https://doi.org/10.26799/cp-nanotechme2017

hydrothermal decomposition [12] and photocatalytic degradation suffers from high capital and operating cost [5, 13, 22-24]. PNA is resistance to biological degradation [13] due to the presence of nitro group in the aromatic ring which enhances the stability of PNA and the degradation rate is very low, whereas the anaerobic degradation yields nitroso and hydroxylamines compounds which are known to be carcinogenic [8,15].

In recent decades, the so-called advanced oxidation processes (AOPs) have been considered as an innovative technology, for the degradation and mineralization of organic pollutants, especially where the refractory species are difficult to remove using biological or physicochemical processes. The process involves the formation of acoustic cavitation in which the heat generated from the cavity implosion activates the extremely reactive hydrogen atoms (H^+) and hydroxyl radicals (OH^-) and both radicals recombines to form hydrogen peroxide (H_2O_2) and molecular hydrogen (H_2) in cooling phase [25]. Sonication influences both oxidation and reduction reaction processes which in turn increases the degradation efficiency of the pollutant molecule [26-28]. It also increases the catalyst active surface area due to particle fragmentation and deagglomeration by increasing the turbulence in the liquid and thus decreasing mass transfer limitations [29].

Heterogeneous Fenton-like systems are active for the degradation of organic compounds, consisting of catalysts and hydrogen peroxide, [30, 31]. Han et al. have proved that the performance of Au/hydroxyapatite (Au/HAp) catalyst for the complete oxidation of organic pollutants in aqueous media by peroxidation and which exhibits high activity and great potential. They have proposed that the catalytic decomposition of H_2O_2 produces hydroxyl (·OH) and perhydroxyl radicals (HO_2) which induces the redox process Au (0) ↔Au (&+) during the wet peroxidation. Zelmanov et al. have used Iron (3+) oxide-based nanoparticles as catalysts in advanced organic aqueous oxidation and gained high efficiency in the oxidation of ethylene glycol and phenol [32].

Recent studies on the degradation of PNA by photocatalysis [14], Fenton oxidation process [13], Oxidative decomposition by solar photo-fenton AOPs [7], transient and steady state photolysis [5] and oxidation of persulfate/Fe_3O_4 [33] have shown that the degradation of PNA was not economical for the industrial application. The main disadvantages of photo-fenton, Photolysis and oxidative decomposition might be high energy consumption of electrical lamps, high capital cost and operating cost. Therefore, the intent of this work was to explore the application of the heterogeneous fenton like system using ultrasound as an advanced oxidation process in activating periodate for the degradation of PNA in water. The effects of experimental parameters such as initial solution pH, FFGN dose, PNA concentration and sodium periodate concentration were investigated.

2. Methodology

2.1. Materials

The following chemicals were used for this study: Iron (II) sulfate heptahydrate ($FeSO_4.7H_2O$, Merck), sodium hydroxide (NaOH, Merck), Ethanol (C_2H_5OH, Changshu Hongsheng), p-nitroaniline ($C_6H_6N_2O_2$, SRL), sodium metaperiodate (NaIO4, SRL) and guar gum (Himedia) and concentrated sulfuric acid (H_2SO_4, Merck). All chemicals were used as received without any further purification and the solutions were prepared using Millipore water (Microcaya-Aquelix5). The ultrasonic processor (Sonics Vibra cell, VCX 500) with a titanium horn (Ti-6Al-4V) of 5cm^2 irradiating surface area, 20 kHz frequency and variable power upto 500W was used for this study.

2.2. Synthesis of Ferroferric oxide-Guaran Nanocomposite:

For the synthesis of Ferroferric oxide-Guaran nanocomposite (FFGN), a natural polysaccharide; Guaran was used as a substrate which acts as stabilizing and capping agent. The hydrolyzed Guaran was used for the synthesis of FFGN, typically 2.78g (1M) of $FeSO_4.7H_2O$ was dissolved in 100mL distilled water, then 9mL of 3M NaOH was injected to the reaction mixture ultrasonication was done using an ultrasonic processor with amplitude of 40% (i.e., 200W).Then, the Guaran with 0.1g concentration was added to the mixture. The reaction was continued for 60 min and ultrasonication was halted when the solution turned from blue to black color which confirms the formation of the magnetite phase. The as-synthesized iron oxide nanocomposite was washed several times in water and dried in a vacuum oven at 120°C. The reaction was carried out in inert atmosphere with nitrogen purged continuously throughout the process.

2.3. Characterization of synthetic Ferroferric oxide-Guaran Nanocomposite:

DOI: https://doi.org/10.26799/cp-nanotechme2017

The crystal structure of the as-synthesized nanocomposite was analyzed by X-ray diffractometer (XRD; Ultima IV, Rigaku, Japan) with X-ray source emitting Cu Kα radiation (k = 1.540562 Å) and scans acquisition at 2θ range from 20° to 80°, scan speed of 1°/min and step size of 0.05°. The operational voltage and current were kept at 40 kV and 300 mA, respectively. The structural morphology of the FFGN were characterized using field emission scanning electron microscopy (FESEM; Zeiss Zigma) with a resolution of 1.3 nm at 20 kV, acceleration voltage of 0.1-30 kV, magnification of 12-1Mx.

2.4. Degradation study:

All the PNA degradation experiments were conducted in a 500 mL cylindrical jacketed reactor, allowing water circulation to maintain the temperature of the reaction solution. To start each test, appropriate volumes of stock PNA and the catalyst FFGN were added into the reactor and then diluted with deionized water to 200 mL. The pH of each reaction solution was adjusted to the desired level by using the prepared 0.1 M sulfuric acid or 0.1 M sodium hydroxide solution, and was measured with a model pHep (Hanna instrument) pH meter. The reaction mixture was subjected to sonication for 120 min and the samples have been taken at regular intervals of 15 minutes for monitoring the oxidation of PNA. The UV–vis spectra of PNA were recorded using a UV–vis spectrophotometer (shimadzu UV2600). The maximum absorbance wavelength (λ_{max}) of PNA can be found at 380 nm from the spectra. Therefore, the concentration of the PNA in the reaction mixture at different reaction times were determined by measuring the absorption intensity at λmax = 380 nm. The 50ppm PNA solution with the solution pH of 6.0 and at the optimal pH of 3.0 was subjected to simple ultrasound irradiation (25mm diameter probe with 200W set power). The degradation efficiency of the treatment methods were evaluated using Eq.1 with the help of the absorbance value found from the UV-Vis spectrophotometer.

$$\%\boldsymbol{Degradation\ efficiency} = \left(\frac{\boldsymbol{C_i - C_f}}{\boldsymbol{C_i}}\right)\boldsymbol{X\ 100} \qquad (\mathbf{1})$$

where, C_i is the initial PNA concentration and C_f is the final PNA concentration.

3. Results and Discussion

The X-ray diffraction pattern of as-synthesized FFGN sample was shown in Fig.1A. The peaks can be indexed at 30.1°, 35.4°, 43.0°, 53.39°, 56.9° and 62.6° corresponding to the crystal planes of (220), (311), (400), (422), (511), and (440) respectively. The sharper and stronger peaks indicate the formation of iron oxide with a cubic inverse spinel structure, which are consistent with the standard data for magnetite (JCPDS card no. 00-019-0629). Results evidenced the presence of guaran. The crystalline regions of Guaran were seen at the angle (2θ) 28.5°, 29.5°, 34.1°, 38.6°, and 49.6°. The particle Zeta Potential was derived from the electrophoretic mobility at 25±2 °C as shown in Fig.1B. The FFGN were evenly distributed with the PDI at 0.651 and the zeta potential measured was -34.8±0.3 mV whereas the Fe_3O_4 nanocubes were evenly distributed with the PDI at 0.751 and the zeta potential was -16.6±0.3 mV. The stability of the nanocomposites against agglomeration was confined with a large negative zeta potential value.

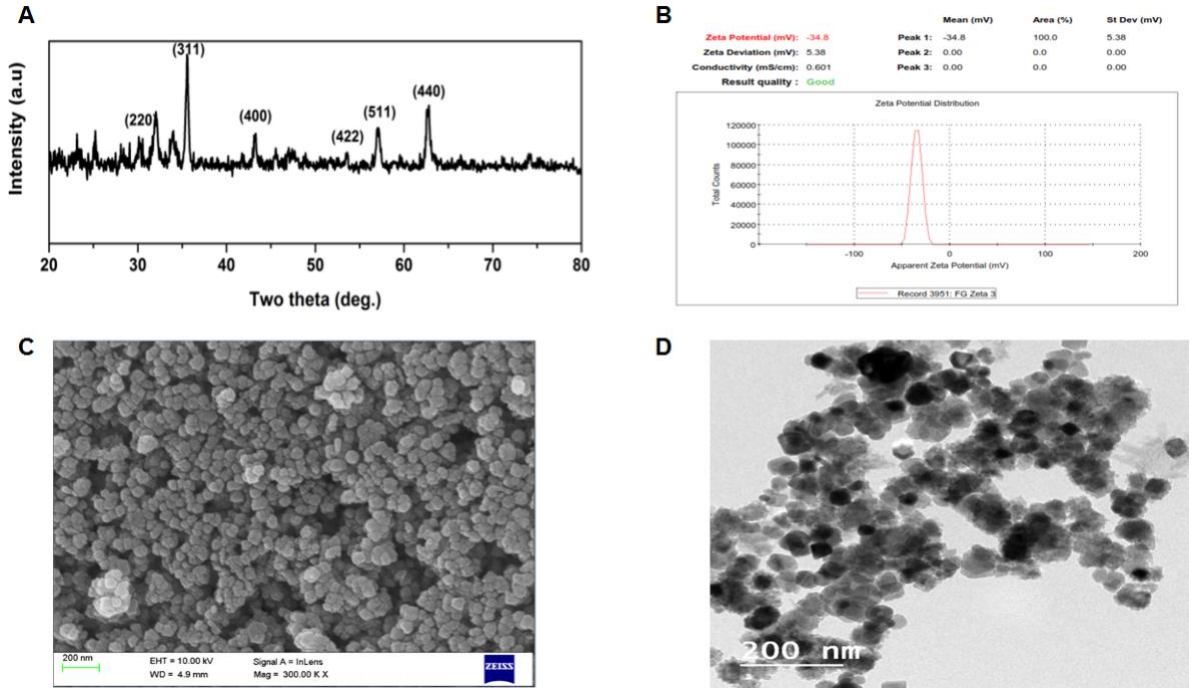

Figure 1. Characterization of the catalyst **A.** XRD, **B.** Zeta Potential, **C.** SEM, **D.** TEM

As shown in Fig.1C reveals that the particles have a relatively narrow size distribution and nearly in uniform cube shape. It also reveals that the FFGN improves the dispersion of nanoparticle and the aggregation of particle was reduced as the guaran coating weakens the magnetic interaction between particles. Fig.1D shows the high-resolution, low magnification images of the as-prepared FFGN, where the cubical shape with well crystallinity are revealed. Polysaccharides as like guaran are highly reactive materials with high oxygen content, thus making them promising O-providers. Guaran are an ideal sustainable substance, certainly "greener" than that of surfactants and additives produced from petrochemical industry. The formed guaran polymer networks expedite the excellent stability and the formation of the NPs through electrostatic and steric effects and the hydroxyl groups of the polymeric chains, would further improve the stabilization of FFGN. The polymer guaran act as a capping agent and the hydroxyl groups of the polymeric chains and networks would surround and protect the particles over longer periods.

The sonochemical degradation of PNA was only 13% at solution pH 8.0 and 33% at pH 3.0 respectively. In the presence of 0.5g/L FGNC catalyst at pH 3.0, it has increased to 47%. The increase in the efficiency was due to the presence of Fe^{2+} ions and the OH^- group in the nanocomposite and the treatment process proceeds rapidly only at pH 3.0. The varying absorbance spectra of the aqueous PNA solution at different treatment conditions were shown in Fig.2.

Proceedings of the Nanotech Middle East 2017 International Conference
Dubai, UAE – December 4 – 6, 2017
DOI: https://doi.org/10.26799/cp-nanotechme2017

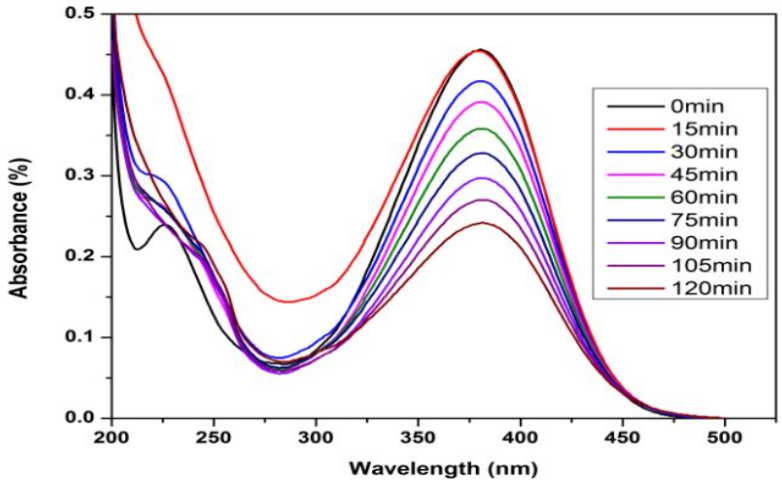

Figure 2. Degradation of PNA plot (pH=3.0± 0.2, FFGN=0.5g/L, $[PNA]_0$=50ppm, Amplitude=40%,Probe=25mm, T=25±1ºC)

The effect of initial concentration of $NaIO_4$ for PNA degradation was performed by varying the $[NaIO_4]_0$ from 0.5g/L to 5.0g/L at the experimental conditions of pH=3.0± 0.2, $[PNA]_0$=50ppm, FFGN=0.1gL, T=25±1ºC and the results are shown in Fig.3A. The degradation rate decreases with the increase in the oxidant concentration. The maximum degradation rate was possible for the oxidant concentration of 0.5g/L, the degradation rate of organic compound decreases with increase of $[NaIO_4]_0$ due to the scavenging of OH^- radical by $[NaIO_4]_0$ and incremental generation of OOH^- radical also consumed.

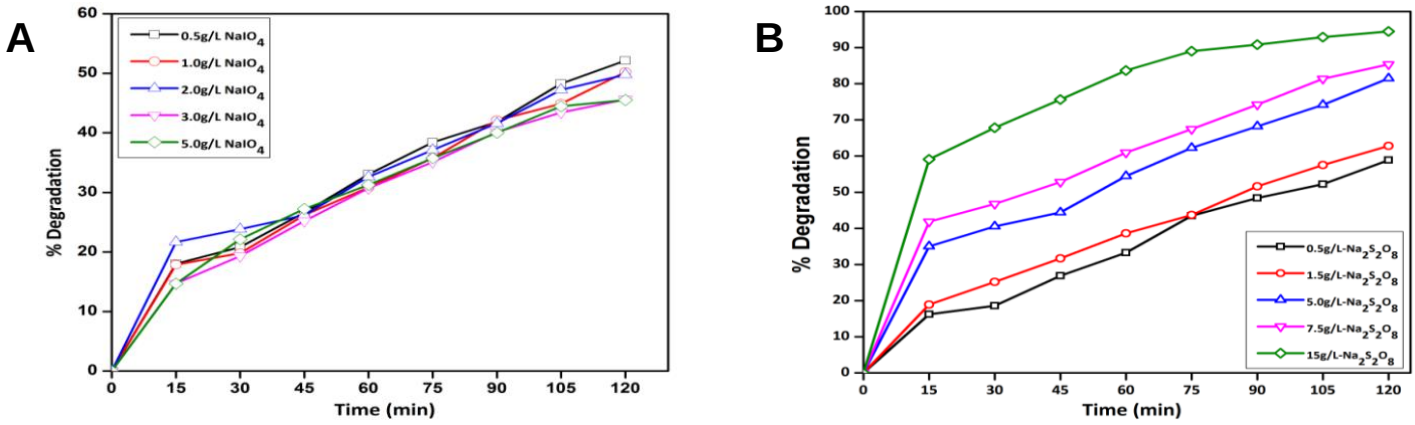

Fig.3. Degradation of PNA plot at different Oxidant concentration (pH=3.0± 0.2, FGNC=0.5g/L, $[PNA]_0$=50ppm, Amplitude=40%,Probe=25mm, T=25±1ºC) **A.** $NaIO_4$ **B.** $Na_2S_2O_4$

The effect of initial concentration of $Na_2S_2O_4$ for PNA degradation was performed by varying the $[Na_2S_2O_4]_0$ from 0.5g/L to 15g/L at the experimental conditions of pH=3.0± 0.2, $[PNA]_0$=50ppm, FFGN=0.5g/L, T=25±1ºC and the results are shown in Fig.3B. The degradation rate was increased from 59% to 94% with the increase of $[Na_2S_2O_4]_0$ concentration. Fe_3O_4 acts as activator in the sulfate-radical based AOP, and it initiates the electron mass transfer of the reacting species (PNA and $Na_2S_2O_4$) which may results in the formation of SO_4^{-*} radical. The SO_4^{-*} radical enhanced the degradation of PNA.

4. Conclusion

The present study reports the green synthesis of FFGN. GG act as a reducing and capping agent. The FFGN nanocubes were synthesized using a cost effective, simple sonochemical method in the absence of any surfactant and

DOI: https://doi.org/10.26799/cp-nanotechme2017

using non-toxic metal salt as reactant. TEM and SEM show that the as-synthesized nanoparticles are cubic in shape with medium particle size of 47 nm. The degradation of PNA by Fenton process was significantly influenced by pH value of the solutions, $[NaIO_4]_0$ and FFGN dosage, initial PNA concentration and the reaction temperature. The optimum conditions for the degradation of PNA in water were considered to be: pH=3.0± 0.2, $[PNA]_0$=50ppm, $NaIO_4$=0.5g/L, Amplitude=40%, Probe=25mm, T=25±1ºC). Under the optimum conditions, the degradation efficiencies of PNA (initial concentration of PNA was 50ppm) were 75% within 120 min reaction. The $NaIO_4$ oxidation of PNA requires large amount of FFGN, which can be easily removed from the reactor at the end of each repetitive oxidation process and that can be used in succeeding runs. Sulfate-radical based oxidation process has many advantages such as being more selective and have longer lifetime compared to $^{-}$OH radical. The optimum conditions for the degradation of PNA in water were considered to be: pH=3.0± 0.2, $[PNA]_0$=50ppm, $Na_2S_2O_8$=15g/L, Amplitude=40%, Probe=25mm, T=25±1ºC). If excess oxidants exist, a quenching reaction of radicals caused by oxidants might occur, which increases the consumption of oxidants for a given concentration of organic contaminants. Under the optimum conditions, the degradation efficiencies of PNA (initial concentration of PNA was 50ppm) were 94% within 120 min reaction. From the above mentioned findings, it is evident that sulfate-radical based oxidation exhibited higher removal efficiency compared to Fenton oxidation process.

References

1. A.S. Travis, Manufacture and uses of the anilines: A vast array of processes and products, the chemistry of anilines. The chemistry of functional groups, Wiley (2007) New York.
2. E. Kavitha, N. Sundaraganesan, S. Sebastin, Molecular structure, vibrational spectroscopic and HOMO, LUMO studies of 4-nitroaniline by density functional method. Indian J Pure Appl Phys 48 (2010) 20-30.
3. V. Shanker, S.M. Rayabandla, R.N. Kumavath, S. Chintalapati, R. Chintalapati, Light-dependent transformation of aniline to indole esters by the purple bacterium Rhodobacter sphaeroides OU5. Curr Microbiol 52 (2006) 413-417.
4. Y.B. Wang, Y.N. Zhang, G.H. Zhao, M.F. Wu, M.F. Li, D.M. Li, Y.G. Zhang, Y.L.Zhang, Electrosorptive photocatalytic degradation of highly concentrated pnitroaniline with TiO2 nanorod-clusters/carbon aerogel electrode under visible light, Sep. Purif. Technol. 104 (2013) 229–237.
5. H.J. Ma, M. Wang, C.Y. Pu, J. Zhang, S.F. Zhao, S. Yao, J. Xiong, Transient and steady-state photolysis of p-nitroaniline in aqueous solution, J. Hazard. Mater.165 (2009) 867–873.
6. H.J. Ma, S. Yao, J. Zhang, C.Y. Pu, S.F. Zhao, M. Wang, J. Xiong, Steady-state and transient photolysis of p-nitroaniline in acetonitrile, J. Photochem. Photobiol. A-Chem. 202 (2009) 67–73.
7. J.H. Sun, S.-P. Sun, M.-H. Fan, H.-Q. Guo, Y.-F. Lee, R.-X. Sun, Oxidative decomposition of p-nitroaniline in water by solar photo-Fenton advanced oxidation process, J. Hazard. Mater. 153 (2008) 187–193.
8. M.A. Oturan, J. Peiroten, P. Chartrin, A.J. Acher, Complete destruction of p-nitrophenol in aqueous medium by electro-Fenton method, Environ. Sci.Technol. 34 (2000) 3474–3479.
9. F. Khan, J. Pandey, S. Vikram, D. Pal, S.S. Cameotra, Aerobic degradation of 4nitroaniline (4-NA) via novel degradation intermediates by Rhodococcus sp strain FK48, J. Hazard. Mater. 254 (2013) 72–78.
10. A. Khalid, M. Arshad, D.E. Crowley, Biodegradation potential of pure and mixed bacterial cultures for removal of 4-nitroaniline from textile dye wastewater, Water Res. 43 (2009) 1110–1116.
11. V. Reddy, R.S. Torati, S. Oh, C. Kim, Biosynthesis of gold nanoparticles assisted by Sapindus Mukorossi Gaertn. Fruit pericarp and their catalytic application for the reduction of p-nitroaniline, Ind. Eng. Chem. Res. 52 (2013)556–564.
12. D.S. Lee, K.S. Park, Y.W. Nam, et al., Hydrothermal decomposition and oxidation of p-nitroaniline in supercritical water, J. Hazard. Mater. 56 (1997) 247–256.
13. J.H. Sun, S.P. Sun, M.H. Fan, A kinetic study on the degradation of p-nitroaniline by Fenton oxidation process, J. Hazard. Mater. 148 (2007) 172–177.

DOI: https://doi.org/10.26799/cp-nanotechme2017

14. S. Gautam, S.P. Kamble, S.B. Sawant, Photocatalytic degradation of 4nitroaniline using solar and artificial UV radiation, Chem. Eng. J. 110 (2005)129–137.
15. A.Saupe, High-rate biodegradation of 3- and 4-nitroaniline, Chemosphere 39 (1999) 2325–2346.
16. K. Zheng, B.C. Pan, Q.J. Zhang, Enhanced adsorption of p-nitroaniline from water by a carboxylated polymeric adsorbent, Sep. Purif. Technol. 57 (2007) 250–256.
17. Y.Q. Wu, M. Zhou, M.G. Ma, et al., Adsorption kinetics of p-nitroaniline on the insolubilized humic acid, Technol. Water Treat. (Chin.) 33 (2007) 14–17.
18. M.G. Ma, Y.X. Wei, Y. Zhang, et al., Modify of clinoptilolit (from Baiyin) and its adsorption of p-nitroaniline, J. Anhui Agri. Sci. (Chin.) 35 (2007) 2061–2062.
19. L.R. Shen, P.Z. Yang, L.Y. Chen, Treatment of waste water containing p-nitroaniline with emulsion liquid membrane process, Technol. Water Treat.(Chin.) 23 (1997) 45–49.
20. K.Q. Li, Z. Zheng, J.W. Feng, J.B. Zhang, X.Z. Luo, G.H. Zhao, X.F. Huang, Adsorption of p-nitroaniline from aqueous solutions onto activated carbon fiber prepared from cotton stalk, J. Hazard. Mater. 166 (2009) 1180–1185.
21. K. Zheng, B. Pan, Q. Zhang, W.M. Zhang, B.J. Pan, Y.H. Han, Q.R. Zhang, D. Wei,Z.W. Cu, Q.X. Zhang, Enhanced adsorption of p-nitroaniline from water by a carboxylated polymeric adsorbent, Sep. Purif. Technol. 57 (2007) 250–256.
22. W.M. Wu, G.D. Liu, S.J. Liang, Y. Chen, L.J. Shen, H.R. Zheng, R.S. Yuan, Y.D. Hou, L. Wu, Efficient visible-light-induced photocatalytic reduction of 4nitroaniline to p-phenylenediamine over nanocrystalline PbBi2Nb2O9, J.Catal. 290 (2012) 13–17.
23. W.M. Wu, S.J. Liang, Y. Chen, L.J. Shen, H.R. Zheng, L. Wu, High efficient photocatalytic reduction of 4-nitroaniline to p-phenylenediamine over microcrystalline SrBi2Nb2O9, Catal. Commun. 17 (2012) 39–42.
24. W.M. Wu, L.R. Wen, L.J. Shen, R.W. Liang, R.S. Yuan, L. Wu, A new insight into the photocatalytic reduction of 4-nitroaniline to p-phenylenediamine in the presence of alcohols, Appl. Catal. B-Environ. 130 (2013) 163–167.
25. K.S. Suslick, The Chemical Effects of Ultrasound, Scientific American (February 1989), pp. 80–86.
26. N.J. Bejarano-Pérez, M.F. Suárez-Herrera,Sonophotocatalytic degradation of congo red and methyl orange in the presence of TiO2 as a catalyst Ultrason. Sonochem. 14 (5) (2007)589–595.
27. I.Z. Shirgaonkar, A.B. Pandit,Sonophotochemical destruction of aqueous solution of 2,4,6-trichlorophenol, Ultrason. Sonochem. 5 (2) (1998) 53–61.
28. D.E. Kritikos, N.P. Xekoukoulotakis, E. Psillakis, D. Mantzavinos,Photocatalytic degradation of reactive black 5 in aqueous solutions: Effect of operating conditions and coupling with ultrasound irradiation, Water Res. 41(10) (2007) 2236–2246.
29. C. G. Joseph, G. L. Puma, A. Bono and D. Krishnaiah, Sonophotocatalysis in advanced oxidation process: A short review, Ultrasonics Sonochemistry 16 (2009) 583–589.
30. M.D.R. Pizzigallo, P. Ruggiero, C. Crecchio, Oxidation of chloroanilines at metaloxidae surfaces, J. Agric. Food Chem. 46 (1998) 2049–2054.
31. H.P. Nguyen, T.K.H. Tran, V.T. Nguyen, Characterization and activity of Fe-ZSM5 catalysts for the total oxidation of phenol in aqueous solutions, Appl. Catal.B-Environ. 34 (2001) 267–275.
32. G. Zelmanov, R. Semiat, Iron (3) oxide-based nanoparticles as catalysts in advanced organic aqueous oxidation, Water Res. 42 (2008) 492–498.
33. Y.S. Zhao, C. Sun, J.Q. Sun, R. Zhou, Kinetic modeling and efficiency of sulfate radical-based oxidation to remove p-nitroaniline from wastewater by persulfate/Fe_3O_4 nanoparticles process. Separation and Purification Technology 142 (2015) 182–188.

Proceedings of the Nanotech Middle East 2017 International Conference
Dubai, UAE – December 4 – 6, 2017
DOI: https://doi.org/10.26799/cp-nanotechme2017

A Study of tribological behavior and lubrication mechanism of graphene nanoplatelets under different lubrications on hvof sprayed wc-co-cr coating deposited on titanium substrate

Y.Sidra[1], M.Abdul[2],kulsoom.I[3]

Institute of Space Technology, Islamabad, Pakistan

Abstract
Degradation by different types of wear has been the major problem in various engineering applications in which different parts operate in severe and drastic conditions e.g. high temperature, moisture and humidity, environmental instability etc. Therefore, WC-Co-Cr HVOF based thermal spray coatings are deployed in a multi range of applications to give extension and long life to components by retarding their wear and corrosion.

The tribological behavior of graphene nanoplatelets in different lubrications was investigated under different lubrication regimes. A ball on disk tribometer has been used at 30N and sliding speed of 0.2m/s for 10min to verify the friction and wear reduction due to graphene nanoplatelets on HVOF sprayed WC-CoCr coating. Their good antiwear and friction properties are due to their laminated structure, which offers the least contact between the two interfaces by providing low shear stress. Furthermore, the results clearly showed that HVOF coating can be protected from wear and friction loses due to the protective tribofilm formed with graphene nanoplatelets under different lubrications.

Keywords: Engine oil, Graphitic nanoplatelets, High velocity oxy-fuel, Lubricating mechanism, Nano-additive engine oil, WC-Co-Cr coatings, Wear rate.

Introduction

The application of the engineered surfaces depends on compatibility to the counter surfaces. Minimizing machine failure, energy loss, friction and mechanical wear failure by lubrication and to enhance service life is a challenging situation for researchers and scientists. Reduction in wear and friction mainly depends on conditions such as, relative motion between the surfaces, sliding speed, normal load, vibration, temperature and lubrication etc.[1]

A surface is itself a defect and regardless of its ultimate finished form it always has depressions, valleys and ridges.[2] So, lubrication with a better nano additive provides the effective mechanical functioning along with improved energy efficiency and durability. Severe tribological conditions exists in military combat operations, aircraft, automotive industries, an efficient lubricant is demanded always.

Control over wear and friction losses using conventional lubricants was a long-ago practice in many applications.[3] But the conventional lubricants are unsatisfactory for the use of commercial applications because of pungent odor, bad thermal stability, and corrosion as it contains sulphur and phosphor.[4] Therefore, quest for nano particles as new kind of additive for lubrication for systemic control over wear and friction has significantly increased from the past few years.[2] Certain nanoparticles such as, metal sulfides,[5] metal oxides,[6] carbon materials, organic material etc. have been investigated as anti-wear agents. Studies have shown the superior lubrication and tribological properties of nano additives than conventional lubricant solid additive. Advantage of using nano additive lubricant over conventional lubricants as anti-wear agents are size and shape effect, enter contact asperities, better chemical reactivity, better protective film, third body effects, limited tribo-chemical reactions etc. These nano additives are added in a low concentration to the base oil (synthetic oil, mineral oil) and brings improvement in the tribological characteristics and presenting good wear and friction reduction effects.

1
2
3

DOI: https://doi.org/10.26799/cp-nanotechme2017

Several anti -wear and frictional mechanisms are reported in the previous papers using titanium dioxide nanoparticles,[7] graphene, graphene flakes, tungsten disulphide etc.

Nano carbon materials have received great attention by tribology researcher due to high load carrying capacity, high chemical stability, strong intramolecular bond, and low surface energy. For practical applications, graphene nanoplatelets have been the focus of interest due to its remarkable properties and unique structure. However, few studies on graphene nanoplatelets have been reported so far. Graphene nanoplatelets have been used for better lubricity and wear resistance properties when used as an oil additive. Huang et al.[8] investigated the frictional behavior and anti-wear property of paraffin oil when graphite nano sheets were added. Lin et al.[9] investigated the tribological properties of graphite nanosheets as an oil additive. Weak intermolecular forces (Vander wall forces) exists between the layers, that enhanced that anti-wear properties. Better friction properties of oleic acid is obtained when graphene sheets were dispersed in lubricant oil.[9] Prasad et al.[10] investigated sliding wear behavior of gray cast iron at different loads using mineral oil additive graphite nanoparticles. At low concentration (5wt%) decrease in wear rate is noticed, while when the concentration is increased to 10wt% the wear rate significantly decreased at high loads. Hwang et al.[11] found the improvement in friction reducing and antiwear property of mineral oil when graphite nanoparticles were added. These spherical shaped nanoparticles prevented direct contact between the sliding surfaces.

The literature review shows that less work has been done on improving the tribological properties of HVOF sprayed WC-10Cr-4Co coatings with lubrications added graphene nanoplatelets.

Therefore, the objective of this paper is to investigate the tribological properties of HVOF sprayed WC-10Cr-4Co coatings under different lubrication conditions with graphene nanoplatelets and reveal the lubrication mechanism of graphite nanoplatelets.

Experimental Details

Sample formulation (Lubrication samples)

Graphene nanoplatelets-GrNP (Purity>99.5wt%, <20 layer, thickness: 4-20nm, Size 5-10µm) purchased from Chengdu Organic Chemicals Co. Ltd., Chinese Academy of Sciences were used throughout the experimental work. API 20W-50 CH-4, SL engine oil was used as a baseline lubricant in this experiment. The samples were prepared with as purchased GrNP with different lubricants using ultrasonication, leading to samples of desired percentage of 0.25wt% concentration. The samples with concentration of 0.25wt% were prepared at ambient temperature in DI water, 20W-50 engine oil, ethanol by dispersing GrNP in 0.0625 g/L of DI water, 0.0625 g/L of engine oil, 0.0625 g/L of ethanol into them. Then mixed ultrasonically (50% amplitude, 2s pulse, 50Hz frequency) for 1hr,30min for DI water +GrNP to make sure that GrNP is well dispersed[12]. The lubricant (20W-50 engine oil) without GrNP was used as a baseline in this work.

The properties of Graphene nanoplatelets and engine oil are listed in the Tables 1 and 2

DOI: https://doi.org/10.26799/cp-nanotechme2017

Table 1: Properties of Graphene nanoplatelets

Graphene Nanoplatelets	**Properties**
Average size (µm)	5-10
Purity (%)	99.5
Thickness (nm)	4-20
Layers	<20
Density (g/cm^3)	0.6
PH Value (30°C)	7.00-7.65

Table 2: Properties of Engine oil

Properties	**Test Method**	**API CH-4/ 228.1, SL**
SAE Viscosity grade		20W-50
Kinematic Viscosity (@40˚C)	ASTM D 445	162
Kinematic Viscosity (@100 ˚C)	ASTM D 445	18.9
Dynamic Viscosity (@-15 ˚C)	ASTM D 5293	8400
Viscosity Index	ASTM D 2270	134
Flash Point -˚C	ASTM D 92	246
Pour point -˚C	ASTM D 97	-27
Color	ASTM D 1500	L 4.0
Density (@15 ˚C) kg/l	ASTM D 4052	0.893
Zinc (wt. %)		0.119

HVOF sprayed WC-Co-Cr coating sample

Cermet powder with the particle size(-45+11µm) was purchased from Guangzhou Sanxin Metals S&T was used for HVOF sprayed WC-Co-Cr coatings. Titanium substrate plates were sand blasted to enhance the mechanical interlocking of powder to the substrate. Coating was deposited with HVOF Sulzer Metco with water cooled diamond jet gun DJ8A hardware 2600, with high pressure, high velocity flame spraying torch which operates at reduced temperature. The fuel used throughout the experiment was hydrogen.

Tribological test

A pin-on-disk tribometer 10.2. friction and wear tester, was used to study the tribological properties of lubricants effect on HVOF sprayed WC-Co-Cr coating.

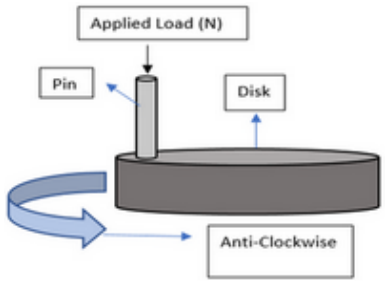

Figure 1:Schematic Diagram of Pin-on-disk Test

The pin-on-disk tests were performed against a 3mm steel as a counter-part acting in relative to the loaded coated HVOF sprayed WC-10Co-4Cr disk. Before wear test the surface of the disk was ground with 800 and 1000 mesh sandpaper, respectively. The basic composition and spraying parameters of a disk are given in table 3 and 4.

DOI: https://doi.org/10.26799/cp-nanotechme2017

Table 3: Spraying Parameters

Flow Rate	10.84L/min
Powder Feed	5.1rpm
Spraying distance	300mm
Flame temperature	2500K

Table 4:Composition and mechanical properties

Composition	WC:86%,Co:10%,Cr,4%
Particle size	-45+11μm
Shape	Spherical
Density	$14.5 g/cm^3$
Hardness	900VHN

The sliding wear resistance of the samples were tested under dry condition and with graphene nanoplatelets added lubrications. The experimental conditions are given in table 5.

The friction co-efficient, wear volume, wear rate was recorded automatically during the test, with the built-in channels of tribometer. The topographical images of wear scars and wear track diameter of disk were observed using scanning electron microscope. Energy dispersive microscopy (EDS) was used to determine the content of elements present on the surfaces of wear scars. Wear surface was characterized by optical microscope (OM) to detect the wear scar diameter of each sample. The experimental conditions are given in table below.

Parameters	**Values**
Normal load (N)	30N
Abrasive material	Diamond pin
Test duration	10 min
Sliding velocity	0.2m/s
Temperature	Ambient
Lubricants	Engine Oil, Ethanol, DI water modified with Nano-additive (GrNP)
Sliding distance	30m
Type of motion	Relative
Speed	200 rpm

Results and Discussion

Graphene Nano platelets (GrNP) Characterization and WC-10Co-4Cr coating

Figure 1 and 2 showed the SEM images of graphene nanoplatelets and HVOF WC-10Co-4Cr coating. The 'flake-like' morphology of GrNP can be seen in the image. The typical EDS analysis of WC-10Co-4Cr coating is shown in figure.

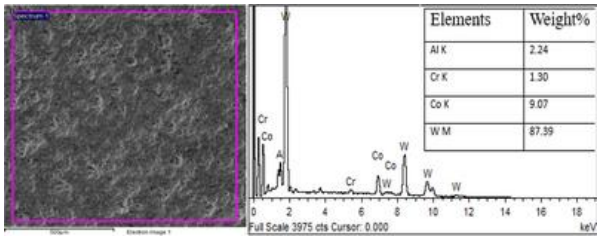

Figure 1: SEM and EDS of HVOF coating WC-10Co-4Cr

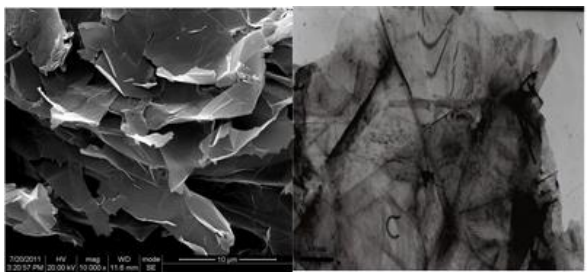

DOI: https://doi.org/10.26799/cp-nanotechme2017

Figure 2: SEM and TEM of GrNP (as received images)

Structure and dispersion stability of GrNP

The as-prepared GrNP was dispersed in DI water, ethanol and 20W-50 SL base oil to a nominal concentration of 0.25wt% with the aid of ultrasonication, and the dispersion were allowed for seven days.[13] Figure 1 (a) shows the pictures of all of the dispersions immediately after sonication (20W-50 engine oil+ GrNP and Ethanol+GrNP for 1hr,30min for DI water +GrNP). To identify the degree of dispersion and sedimentation pictures were again taken after 7 days. Just after sonication, GrNP showed good dispersion in water, ethanol as the edges of layers become partially hydrophilic and are well dispersed in water. Water and ethanol exhibit significant dipole moment values and showed good dispersibility due to solvent polarity. While with the base oil, the multilayered GrNP showed good dispersion without surface modification or adding any surfactants. Moreover, it is evident that carbon-based materials stability in an aqueous medium is highly dependent on the hydrophilic functional group, which interacts with the repulsive force (columbic) and hydrogen bonding. Therefore, for GrNP, the defect on its edges contain unfilled carbon bonds that assist in providing favorable sites for oxidative reaction. Thus yielding more hydrophilic structures which comprises of various functional groups (water based), such as ethers, carboxyl and hydroxyls. [14, 15]Thus its solubility is size-dependent since more functional exists in larger sheets, which contains structural defects.

The good dispersing stability of lubricants can be explained by the following

1) Ultrasonication highly eliminated the hydrophobicity of basal plane layers, and brings oxidative reaction and more hydrophilic sites at the edges.
2) At higher temperature, Brownian motion of lubricants is increased and this helps in the dispersion of GrNP.

After 7 days, the picture showed the sedimentation and settling of GrNP in 3 lubricants.

The rate of settling is highly dependent on the density difference between the GrNP and viscosity of lubricants etc. The interaction potential and forces between the layers, attracts each other and agglomeration occurs. Density of fluids plays an important role in agglomeration of GrNP.

Figure 2: DI+GrNP ,b)GrNP+Oil, c)base oil, d) ethanol+GrNP

Day 7

Figure 3 :a) DI+GrNP ,b)GrNP+Oil, c) base oil , d) ethanol+GrNP

Tribological characteristics and characterization

Influence of Graphene Nanoplatelets on Friction-Reducing capability of lubricants

DOI: https://doi.org/10.26799/cp-nanotechme2017

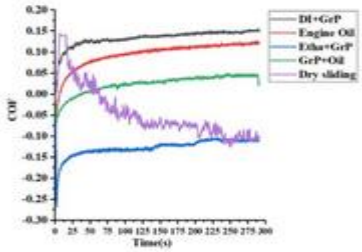

Figure 4: variation of friction coefficient with friction time for various lubrication conditions

Figure 4 shows the variation of friction coefficient with friction time for various lubrication conditions It can be seen from Figure 3 that, under dry friction condition, with the increase of friction time, friction coefficient increased firstly, then decreased, and eventually reached a quasi-steady state. The increase of COF is due to the continuous generation of wear debris in the form of hard particles entrapped between the worn surfaces. Plastic deformation process increases the hardness of the debris particles and they scrape the surrounding material. COF then reached to negative value, suggested that, thick oxide layer formed on the surface due to oxidation. The oxide formed on the surface adhere to the surface as thick layer and provide protection against the sliding asperity.

Under lubrication conditions the behavior of each specimen on coating was different while following the same pattern i.e. increased firstly with friction coefficient and then reached a stable state value. Etha+GrNP showed the lowest values of friction coefficient (-0.13) values than the rest of the specimens. This COF reduction with friction time is thought to be the combined lubrication effect of ethanol and layered structure of GrNP. While test performed with base oil without GrNP showed the high COF (0.11), suggesting that graphene nanoplatelets is most likely the reason for the friction reduction. This can also be the suggested that on contact with the counter body local surface temperature rise occurred due to low thermal conductivity that reduces the viscosity of oil to some extent as compared to GrNP+Oil. The fairly stable COF attained is due to the graphitic layers entrapped in the contact area is high and continuous lubricating film comprising of graphene was formed on the surface. While during sliding the initial graphene layers was removed quickly out of wear track region and resulted in high COF as happened in DI+GrNP. But after that the thin laminated layer structure fills up grooves along with self-lubrication avoids the direct contact between the two rubbing surface[15].Low concentration of GrNP in solution forms a protective tribofilm, resulting in low and stable COF.

Effect of Rotation speed on friction

To study the tribological properties of the tested lubricants along different lubrication regimes, the experimental approach proposed by Kovalchenko et al. (2005) is adopted for the current study.

The coefficient of friction (COF) values of different lubricants with GrNP and 20W-50 SL base oil, measured using the pin-on-disc tribometer at different sliding velocities for 300s at ambient temperature introduces Stribeck curve given in figure 4.

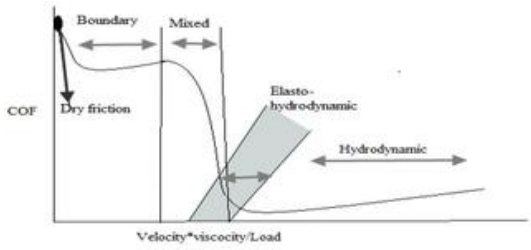

Figure 5: Lubrication regimes

The general form of Stribeck curve proposed by Kovalchenko et al.[16], depicting the lubricating regimes is available for every lubricated system. The friction test begins with an increasing rotating speed until 250rpm for 300s is achieved. The shape of graph shows a transition behavior from dry condition-mixed lubrication regime-elastohydrodynamic lubrication regime (EHL)-hydrodynamic lubrication regime (HL-full film lubrication) for increasing speed.

DOI: https://doi.org/10.26799/cp-nanotechme2017

At lower rotational speed (0-5rpm), specially at transition point B in figure 4, the lubrication regime of ethanol+GrNP, 20W-50 SL base oil, GrNP+Oil is EHL, while DI+GrNP shows mixed lubrication regime. At higher rotating speed all lubricants show the transition to HL i.e. full film lubrication regime, where the friction is determined by the viscosity of laminated GrNP. HH COF of GrNP+Oil and ethanol+GrNP is lowered than 20W-50 SL base oil. This might be attributed to the exposure of GrNP lamellar layers under the applied load. A positive effect of GrNP on lowering the friction coefficient is specially observed in EHL regime where the viscous stress is prevalent. Moreover, increase in COF in HL regime shows that after a transition from EHL to HL, lubrication suffer from wear and some particles worn out from the surface but later form a uniform tribofilm and reduces the energy loss in mechanical lubrication. These tests confirm that using GrNP ion lubricants enhances the friction reduction capability in mixed, EHL and HL regime as reported in[17]

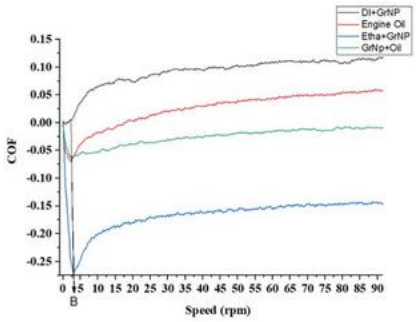

Figure 6: Effect of rotational speed on friction behavior at RT

Influence of Graphene Nanoplatelets on Wear-Reduction capability of lubricants

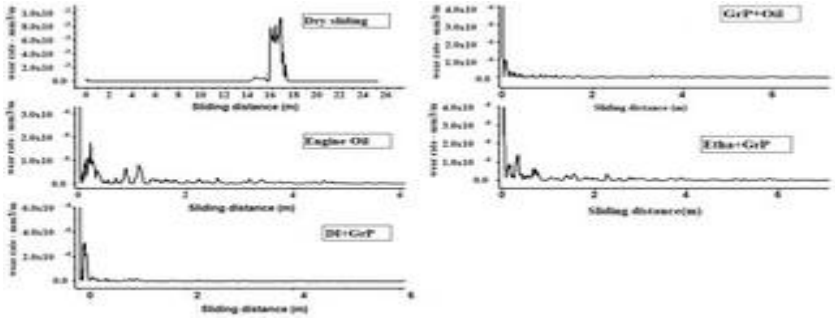

Figure 7: Variation of wear rate with sliding distance for various lubrication conditions

Figure 6 shows the variation of wear rate with sliding distance for various lubrication conditions. The same trend is observed in wear rate, high in the beginning and then decreases with increasing sliding distance. It can be inferred that lubrications with GrNP showed less wear rates as compared to without lubrication due to their thin laminated structure which allows the GrNP to form self-assembled tribofilm and reduces the direct contact between the two surfaces**.** Initial increase in wear rate of DI+GrNP is due to corrosive wear as sliding motion between the surfaces forced some GrNP to lose and rest GrNP formed a tribofilm on the surface with increasing sliding distance. ethanol+GrNP showed uniform distribution of GrNP with the increase in sliding distance after a high wear rate due to high sliding contact pressure that vaporizes the ethanol leaving behind GrNP. Graphene stacking piles takes place and Vander wall forces between different layers helps in the slipping process that lowers the wear rate.[17]Moreover 0.25wt% concentration also effects in lowering wear mechanism.

Observation of wear tracks

Microscopic examination of the wear track showed the presence of important quantities of debris within the wear track. Debris is of whitish color regardless of the lubricant used. Debris is of two kinds flakes or platelets (20W-50 engine oil+ GrNP and ethanol+GrNP, DI+GrNP) and finer particles (20W-50 engine oil)

DOI: https://doi.org/10.26799/cp-nanotechme2017

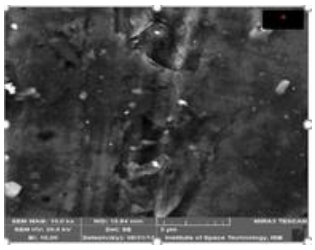

Figure 8:SEM & EDS of GrNP+Oil

Figure 9:SEM & EDS of GrNP+DI

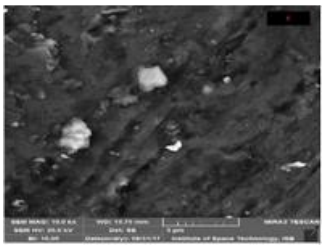

Figure 10: SEM & EDS of GrNP+Ethanol

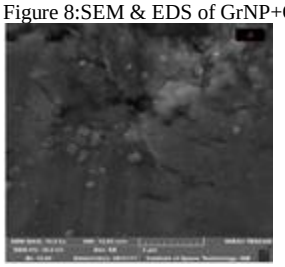

Figure 11: SEM & EDS of GrNP+Ethanol

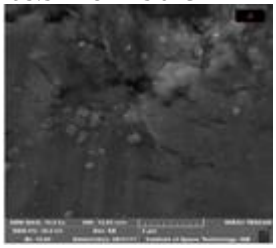

Figure 12:SEM & EDS of Base Oil

From the SEM images, it can be suggested that groove marks are filled with the graphene nanoplatelets provided a decrease in COF and wear rate in 20W-50 engine oil+ GrNP, DI+GrNP, Etha+GrNP. These accumulated platelets act as a load carrying entities and significantly affect the wear rate. In case of base oil, one possible explanation for this behavior may be due to the agglomeration and accumulation of GrNP occurs in the contact area. This reduces the lubricating effect of solution and micro plowing and micro cracking can be seen. Figure 4.15 shows plowing traces, spalling, deformation and cracks on the wear surface of the coating under dry condition. This indicates that coating suffers from severe damage without lubrication at 30N load.

The examination of the worn surface has thus allowed the detection of the presence of platelets in either form i.e. particle or agglomerated debris. The debris contributed to the wear process through the following mechanism.

1) Micro-cracking and micro-plowing along the sliding contact (20W-50 engine oil)
2) Abrasion by accumulated platelets and flakes of GrNP and fine debris circulating along the sliding contact (20W-50 engine oil+ GrNP, DI+GrNP, Etha+GrNP).

The lubrication mechanism of lubricants can be confirmed by the results of SEM and EDS. Owing to small size and high surface energy of GrNP, they could stably form a tribofilm on the surface of HVOF coating. The EDS spectra for 20W-50 engine oil+ GrNP, DI+GrNP, Etha+GrNP revealed a C characteristic peak, which indicates that GrNP is transferred to the surface to lubricate the friction pairs.

The presence of Fe and chromium is due to the steel contact with DI, ethanol, base oil. While the oxygen was due to the oxide layer formed in base oil.

Discussion

Debris role in wear Process under lubrication

In hard coatings like cermet coatings, wear debris formation either increase the friction coefficient or increase it along with the increase, decrease of wear rate. Wear debris acts in a dual manner such as;

1) Its interaction with the sliding surface either by plowing and abrasion, increases the COF.
2) It acts as a load carrying entities and decreases the wear rate and increases COF. Variation in the behavior of COF depicts the different quantities of debris formation between sliding interfaces. Formation and elimination of wear debris from the wear track conveys dynamic equilibrium in COF behavior. Constant quantity of debris formation at the wear track corresponds to stability of COF, increase in buildup indicates increase in COF, whereas decrease reflects the elimination zone.

DOI: https://doi.org/10.26799/cp-nanotechme2017

Steady-state friction coefficient indicate that the constant quantity of debris is entrapped in the sliding interface. Hence it appeared as if, friction coefficient is independent of applied load and just depends on sliding speed that helps in the circulation of debris across the surface and makes it invariant.

Contact interface behavior under lubrication

Variation in COF thus allows the influence of sliding speed on the wear rate to be explained. First, COF and wear rate exhibit opposite changes with increasing sliding speed. The critical sliding speed provides the maximum COF and minimum wear rate as a result of maximum load carrying effect. The critical speed marks the limit between both phases of debris accumulation and elimination. High critical speed helps in the fine dispersion of lubrication solution with GrNP and stabilizes the COF.

Below critical speed (0.01m/s) ethanol+GrNP, 20W-50 engine oil+ GrNP and base oil showed the initial decrease in COF and hence wear rate increases due to the elimination of debris. This results in reduction in load carrying capacity of debris. The steady state COF after the critical speed showed the accumulation of enough debris that circulates along the sliding direction and makes it invariant.

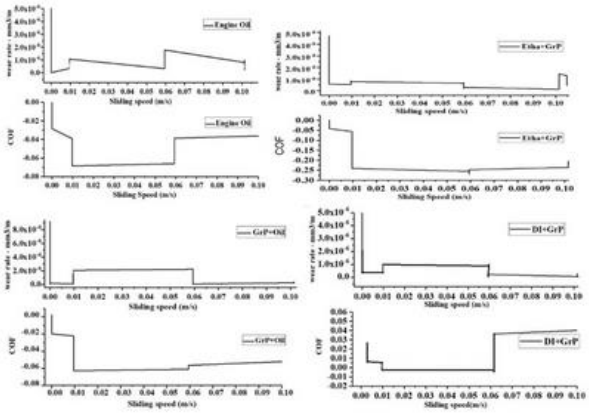

Figure 13:Variation of wear rate & COF w.r.t sliding speed

Conclusion

A series of experiments was conducted to test the wear and friction behavior of HVOF sprayed WC-10Co-4Cr coatings under dry and four different lubricated conditions. Wear of the coating was greatly reduced (few orders of magnitude) with reduction in friction coefficient by the presence of graphene nanoplatelets at the tribological surface as compared to dry condition test.

1) The best antiwear and result has been observed in hydrodynamic, mixed and Elasto-hydrodynamic conditions.
2) The good friction and antiwear properties of graphene nanoplatelets may be due to their multiple layered structure which offers least contact between the two sliding bodies.

Future work

Future work includes

1) Should develop better dispersion methods along with better dispersant for GrNP dispersion in base oil and other solvents.
2) Search for optimal concentration of GrNP in different bases, for better viscosity and better anti-wear property.
3) Search for more nano-lubricating agents which have low surface tension and incorporates in the pores of WC-Co-Cr coating for better wear and corrosion.

References

DOI: https://doi.org/10.26799/cp-nanotechme2017

1. [1] M. A. Chowdhury and M. M. Helali, "The effect of frequency of vibration and humidity on the wear rate," *Wear*, vol. 262, pp. 198-203, 2007.
2. V. Eswaraiah, V. Sankaranarayanan, and S. Ramaprabhu, "Graphene-based engine oil nanofluids for tribological applications," *ACS applied materials & interfaces*, vol. 3, pp. 4221-4227, 2011.
3. K. C. Ludema, *Friction, wear, lubrication: a textbook in tribology*: CRC press, 1996.
4. D. Bokarev, V. Bakunin, G. Kuz'mina, and O. Parenago, "Highly effective friction modifiers from nano-sized materials," *Chemistry and Technology of Fuels and Oils*, vol. 43, pp. 305-310, 2007.
5. S. Chen and W. Liu, "Characterization and antiwear ability of non-coated ZnS nanoparticles and DDP-coated ZnS nanoparticles," *Materials Research Bulletin*, vol. 36, pp. 137-143, 2001.
6. A. H. Battez, J. F. Rico, A. N. Arias, J. V. Rodriguez, R. C. Rodriguez, and J. D. Fernandez, "The tribological behaviour of ZnO nanoparticles as an additive to PAO6," *Wear*, vol. 261, pp. 256-263, 2006.
7. X. Shao, W. Liu, and Q. Xue, "The tribological behavior of micrometer and nanometer TiO2 particle-filled poly (phthalazine ether sulfone ketone) composites," *Journal of applied polymer science*, vol. 92, pp. 906-914, 2004.
8. H. Huang, J. Tu, L. Gan, and C. Li, "An investigation on tribological properties of graphite nanosheets as oil additive," *Wear*, vol. 261, pp. 140-144, 2006.
9. W. Zhang, M. Zhou, H. Zhu, Y. Tian, K. Wang, J. Wei, *et al.*, "Tribological properties of oleic acid-modified graphene as lubricant oil additives," *Journal of Physics D: Applied Physics*, vol. 44, p. 205303, 2011.
10. B. Prasad, S. Rathod, M. Yadav, and O. Modi, "Sliding wear behavior of cast iron: Influence of MoS2 and graphite addition to the oil lubricant," *Journal of Materials Engineering and Performance*, vol. 20, pp. 445-455, 2011.
11. Y. Hwang, C. Lee, Y. Choi, S. Cheong, D. Kim, K. Lee, *et al.*, "Effect of the size and morphology of particles dispersed in nano-oil on friction performance between rotating discs," *Journal of Mechanical Science and Technology*, vol. 25, pp. 2853-2857, 2011.
12. D. W. Johnson, B. P. Dobson, and K. S. Coleman, "A manufacturing perspective on graphene dispersions," *Current Opinion in Colloid & Interface Science*, vol. 20, pp. 367-382, 2015.
13. D. Konios, M. M. Stylianakis, E. Stratakis, and E. Kymakis, "Dispersion behaviour of graphene oxide and reduced graphene oxide," *Journal of colloid and interface science*, vol. 430, pp. 108-112, 2014.
14. L. Rapoport, O. Nepomnyashchy, I. Lapsker, A. Verdyan, A. Moshkovich, Y. Feldman, *et al.*, "Behavior of fullerene-like WS 2 nanoparticles under severe contact conditions," *Wear*, vol. 259, pp. 703-707, 2005.
15. F. A. Vidal and A. F. Ávila, "Tribological investigation of nanographite platelets as additive in anti-wear lubricant: a top-down approach," *Journal of Tribology*, vol. 136, p. 031603, 2014.
16. A. Kovalchenko, O. Ajayi, A. Erdemir, G. Fenske, and I. Etsion, "The effect of laser surface texturing on transitions in lubrication regimes during unidirectional sliding contact," *Tribology International*, vol. 38, pp. 219-225, 2005.
17. A. Senatore, V. D'Agostino, V. Petrone, P. Ciambelli, and M. Sarno, "Graphene oxide nanosheets as effective friction modifier for oil lubricant: materials, methods, and tribological results," *ISRN Tribology*, vol. 2013, 2013.